TWO-PLANE WAVE TOMOGRAPHY AND

LITHOSPHERIC STRUCTURE BENEATH EASTERN TIBET

A Dissertation

presented to

the Faculty of the Graduate School

at the University of Missouri-Columbia

In Partial Fulfillment

of the Requirements for the Degree

Doctor of Philosophy

by

SAVAS CEYLAN

Dr. Eric Sandvol, Dissertation Supervisor

DECEMBER 2013

The undersigned, appointed by the dean of the Graduate School, have examined the dissertation entitled

TWO-PLANE WAVE TOMOGRAPHY AND
LITHOSPHERIC STRUCTURE BENEATH EASTERN TIBET

presented by Savas Ceylan,

a candidate for the degree of Doctor of Philosophy of Geological Sciences,

and hereby certify that, in their opinion, it is worthy of acceptance.

_____

Professor Eric Sandvol

_____

Professor Mian Liu

_____

Professor Robert Bauer

_____

Professor Francisco Gomez

_____

Professor Stephen Montgomery-Smith

ACKNOWLEDGEMENTS

First and foremost, I want to thank my advisor Dr. Eric Sandvol. Starting from my first day as his PhD student, he patiently guided me through challenges of my research. Not only he is a good teacher, but also he has been a great mentor. I extensively benefited from his knowledge and scientific insights. Additionally, I do not know how to thank Dr. Sandvol enough for the field experience I gained over the years I worked with him. I know he thinks he will be free of me finally; but he is wrong.

I also would like to thank all my dissertation committee members and the MU Geology family. Each and every one of them is invaluable for me. I did not have any knowledge of geology before. They collaboratively made me realize how important geology is for a seismologist. Drs. Mian Liu, Robert Bauer, and Francisco Gomez patiently walked me through structural and surficial geology, plate tectonics and geodynamics. Dr. Montgomery-Smith was always supportive and tolerant with my math problems.

Finally, my deepest gratitude goes to my wife, Gina Ceylan, for her patience and support over the last few years. She contributed to every step of my research in many ways. Without our long scientific discussions over long nights, this journey would not be as fun.

TABLE OF CONTENTS

LIST OF FIGURES

TWO-PLANE WAVE TOMOGRAPHY AND LITHOSPHERIC STRUCTURE BENEATH EASTERN TIBET

Savas Ceylan

Dr. Eric Sandvol, Dissertation Supervisor

ABSTRACT

This dissertation focuses on two specific research topics: First, I study the lithospheric structure beneath E. Tibetan Plateau, using new data from INDEPTH-IV (INternational Deep Profiling of Tibet and the Himalayas) seismic experiment. I show new shear wave tomographic maps, in order to better constrain the existing geodynamic models regarding the growth and dynamics of the region. In the second part, I investigate seismic resolution capabilities of the two-plane wave method using synthetic seismograms. Further, I modify and apply this approach to Love waves.

My shear wave tomography results indicate that subhorizontal underthrusting of the Indian plate beneath E. Tibet does not extend much further north of Bangong-Nijuang Suture. Moreover, my tomographic images clearly show that the Indian lithosphere is laterally torn into at least two fragments. The westernmost fragment is detached from the rest of the Indian plate, and vertically sinking into the astenosphere. Azimuthal fast directions are consistent at depth beneath the central part of the study region, suggesting vertically coherent deformation of crust and uppermost mantle. Further, I observe low velocity zones along the northern and southern branches of the Kunlun fault, and I attribute these zones to strain heating due to ductile deformation. Moreover, these low

velocity zones below the Kunlun Shan are continuous at depth, providing evidence against a present southward continental subduction or underthrusting.

One of the most important limitations of seismic tomography studies is spatial resolution of applied methods. To determine the resolution of my tomographic models, I calculate synthetic seismograms for ideally isotropic checkerboard earth models, and apply two-plane wave tomography. My results prove that SV anomalies smaller than the dominant wavelength of surface waves can be recovered down to ~200 km, where traditional approaches break down. For Love waves, a modified version of the approach is required, incorporating two perpendicular components for two plane wave solutions along x and y directions of the local coordinate system. Moreover, the method exhibits adequate resolution for SH waves down to ~100 km. Smearing is more evident in SH results due to shallower depth sensitivity and longer wavelengths of Love waves than Rayleigh waves.

Chapter 1: Introduction

My research focuses on two specific subjects: The first part of my dissertation includes application of two-plane wave tomography (TPWT) [*Forsyth*, 1998] to infer the lithospheric structure beneath Eastern Tibetan Plateau. I use Rayleigh waves for obtaining the shear wave structure beneath the region, incorporating data from Namche-Barwa [*Sol et al.*, 2007] and INDEPTH-IV (**IN**ternational **D**eep **P**rofiling of **T**ibet and the **H**imalayas) seismic experiments (Figure 1.1). Despite many studies over last two decades, the findings and interpretations on the northern extent of the Indian Plate and
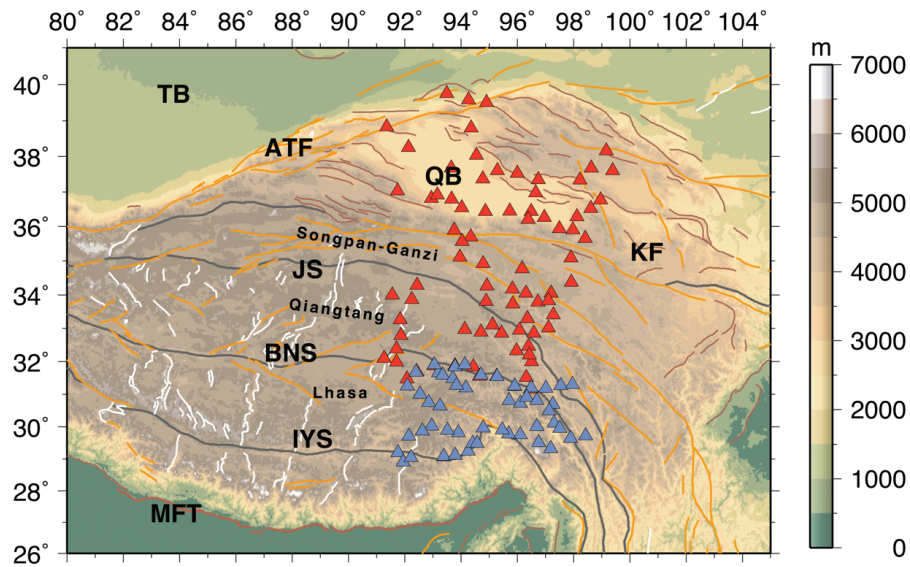
Figure 1.1. Study area with seismic station locations (red triangles are INDEPTH-IV stations, blue triangles indicate Namche-Barwa stations) with tectonic features [*Styron et al.*, 2010]. This figure will also used further in Chapter 2. White and brown lines show normal and thrust faults, respectively. Orange lines represent strike-slip faults. Suture zones are marked by thick gray lines. IYS: Indus-Yarlung suture; BNS: Bangong-Nujiang Suture; JS: Jinsha Suture; KF: Kunlun Fault; QB: Qaidam Basin; TB: Tarim Basin; ATF: Altyn-Tagh Fault; and MFT: Main Frontal Thrust.

lithospheric structure beneath the plateau remain controversial. For instance, surface wave tomography study of *Zhou and Murphy* [2005] proposes wholesale underthrusting of Indian plate beneath E. Tibet [*Argand*, 1924; *Barazangi and Ni*, 1982]. On the other hand, a body wave tomography study along a profile ~1° west of INDEPTH-IV array [*Tilmann et al.*, 2003] reveals a steep underthrusting which ends roughly north of Bangong-Nijuang Suture (BNS). Moreover, contrary to receiver functions study of *Yue et al.* [2012], findings of some studies indicate present-day southward continental subduction south of Qaidam Basin [*Kind et al.*, 2002; *Zhao et al.*, 2011]. One significant cause of these discrepancies in the above findings is poor seismic coverage, i.e. most these studies to date were perfomed along a profile. In my Rayleigh wave tomography study, I use new data from INDEPTH-IV seismic array, which is the largest temporary array deployed (74 stations) in the region to date, with an average inter-station distance of ~80 km (Figure 1.1). My results (Chapter 2) clearly show that underthrusting of Indian plate does not extend much further north of BNS. Further, I propose that the Indian plate is laterally fragmented into at least two wings. Additionally, my tomographic models provide evidence against continental subduction model, south of Qaidam Basin.

The second part of my dissertation (Chapter 3) is more theoretical, and focuses on resolution capabilities of TPWT. The most important limitation of traditional surface wave tomography is that it breaks down when sizes of heterogeneities are comparable to the dominant wavelength of surface waves. In theory, TPWT does not share this limitation; however none of the earlier studies (e.g. *Forsyth and Li* [2005]; *Ceylan et al.* [2012]) attempted to measure true capabilities of the method. Moreover, with the exception of *Li and Li* [2012], there are no studies investigating the method's

applicability to Love waves. In Chapter 3, I use synthetic seismograms to determine resolution capabilities and robustness of TPWT. My results prove that TPWT can recover anomalies approximately half the size of dominant wavelength in the mantle. Moreover, I show that a modified version of TPWT is applicable to Love waves.

This dissertation is structured as follows: In Chapter 1 (this chapter), I provide theoretical background for TPWT. Next, I explain how TPWT works, and avoids the weaknesses of other approaches. Further, I briefly describe seismic anisotropy, and how I account for finite frequency effects using sensitivity kernels. In Chapter 2, I present Rayleigh wave phase wave speed and shear wave results from applying TPWT to E. Tibetan Plateau. Further, I discuss several competing models for growth and deformation of E. Tibet. Finally, in Chapter 3, I address problems with resolution of TPWT by using synthetic seismograms. I demonstrate this method's applicability to Love waves, and reliability for imaging relatively small anomalies. I also explain why TPWT has the capability of recovering anomalies smaller than the dominant wavelength of surface waves.

1.1. Two-plane wave tomography

Seismic surface waves travel parallel to earth's surface, sampling different depths with a range of frequencies. Fundamental mode Rayleigh and Love waves are most sensitive to earth structure at depths corresponding to ~1/3 and ~1/4 of their dominant wavelengths, respectively [*Knopoff*, 1972]. Surface waves are *dispersive*, i.e. relatively longer period surface waves have greater wavelengths, allowing them to travel through deeper parts of the earth at greater wave speeds. Using a range of frequencies, we can

take advantage of surface wave dispersion to calculate phase and group wave speeds as a function of depth. These characteristics of surface waves make them valuable tools for studying earth structure in the crust and uppermost mantle.

One of the earliest attempts at measuring surface wave dispersion include single station method. This method uses only well-dispersed records, relying heavily on the initial phases of waves generated by an earthquake. For this reason, the single station method requires precise knowledge of source parameters. Due to this limitation, it is often unreliable for measuring surface wave dispersion. A more traditional and widely applied technique is the two-station method. This method adapts an approach similar to travel time tomography, employing relative travel times of surface waves between two stations, lying approximately on the same great circle path (within the range of ±15°). One advantage of this approach is ease of implementation, as the forward problem of surface wave propagation is reduced to seismic ray theory, which assumes seismic waves consist of infinite frequencies. However, surface waves have finite frequencies. Therefore, traditional surface wave tomography breaks down when the wavelengths of heterogeneities are similar to wavelengths of surface waves [*Li*, 2011; *Zhou et al.*, 2004]. Additionally, lateral heterogeneities between events and seismic arrays may cause scattering and multipathing. Consequences of these finite frequency effects include distortion of ray paths and variations in amplitudes [*Forsyth and Li*, 2005]. For these reasons, amplitude information is ignored in traditional methods. Moreover, since the traditional method requires stations to be on the same great circle path as events, not all the station-event pairs can be included in tomographic inversions. Therefore, resolution

and robustness of phase velocity measurements are highly affected by number and spatial
distribution of ray paths.

TPWT [*Forsyth*, 1998] does not share these limitations. Rather, it uses both
amplitude and phase variations, assuming that distortion of a wavefront at any location
within a seismic array (i.e. receiver locations and inversion nodes) can be expressed as
the sum of two plane waves [*Forsyth*, 1998; *Forsyth and Li*, 2005]. This assumption can
be expressed as follows:

$$
{}_i^k U = {}_i A_1 \exp\left(-i\,{}_i^k\phi_1\right) + {}_i A_2 \exp\left(-i\,{}_i^k\phi_2\right), \tag{1.1}
$$

where U is the displacement at k^{th} station caused by i^{th} event, and A and ϕ are amplitudes
and phases of two plane waves, respectively. Further, the phase (ϕ) terms in Equation
(1.1) can be expressed as:

$$
{}_i^k\phi_{1,2} = {}_i^0\phi_{1,2} + \overline{{}_i^k S}\,\omega\left\{{}_i^k r\cos\left({}_i^k\psi - {}_i\vartheta_{1,2}\right) - {}_i^k x\right\} - \omega\left({}_i^k\tau - {}_i^0\tau\right) \tag{1.2}
$$

where ${}_i^0\phi_{1,2}$ represents phases of first and second plane waves at a reference station, and
$\overline{{}_i^k S}$ is the average slowness. ${}_i^k\tau - {}_i^0\tau$ is the difference between travel times along the great
circle path, measured from the edge of study area to the kth and reference station. ${}_i\vartheta_{1,2}$
denotes deviation from the great circle path for both plane waves [*Forsyth and Li*, 2005].
Hence, the wavefield at each station for a single frequency can be described by three

unknowns for each plane wave: relative amplitudes and phases with respect to a reference

station, and deviation angles from the great circle path.
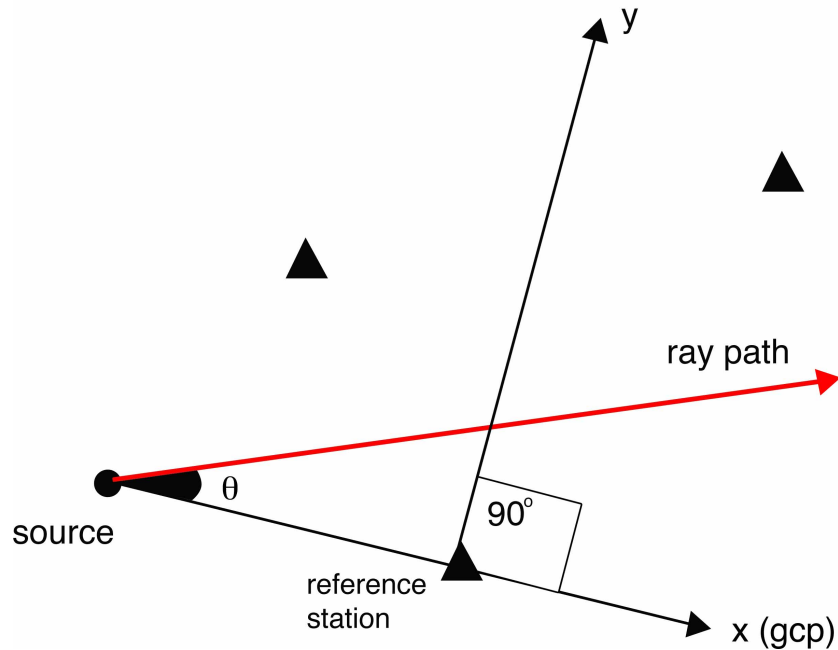
Figure 1.2. A schematic of local Cartesian coordinate system. The reference station is chosen using the minimum RMS misfit in amplitude with respect to mean value, x-axis is along the great circle path (gcp) with the source, and y-axis is 90° counterclockwise. Triangles show stations. The distance between source and center of seismic array is greater than 20°.

To invert for these unknowns, a local Cartesian coordinate system is set up for

each event (Figure 1.2), where reference station is the origin, x direction is along the

great circle path between source and reference station, and y direction is 90°

counterclockwise from x. The reference station is determined using the lowest root mean

square error of amplitudes with respect to the mean value. Alternative methods for the

reference station decision include using the shortest event-receiver distance or maximum

amplitude.
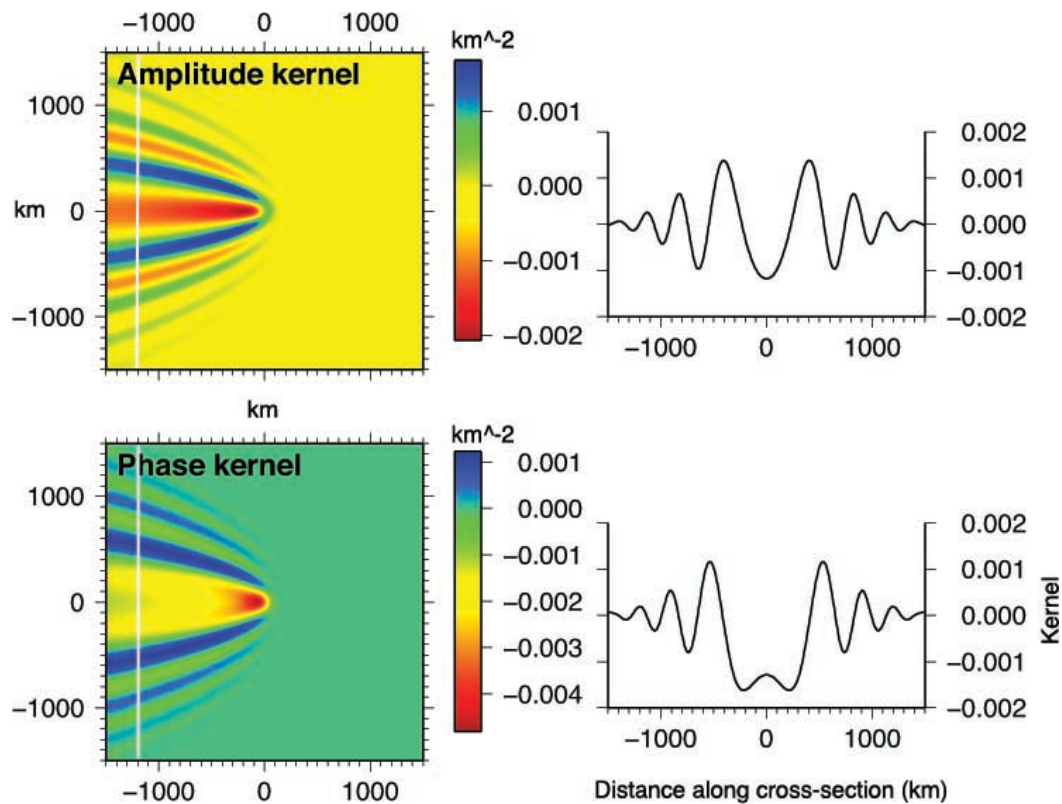
Figure 1.3. Map views of amplitude and phase sensitivity kernels for 20 mHz Rayleigh waves, obtained using Born approximation. Panels on the right side show cross-sections along -1200 km (white solid line on map views). The hypothetical station is located at the center, and source is to the west.

Following the standard procedure, I calculate phase wave speeds using both Rayleigh (vertical component) and/or Love (transverse component) waves for a set of frequencies at defined points within a study area. Then, I use these 1D dispersion results for obtaining a 3D shear wave structure. More specifically, I employ DISPER80 algorithm [*Saito*, 1988] for each individual dispersion curve to obtain 1D shear wave profile. Next, these shear wave profiles are combined to construct a 3D model. To

7

account for finite frequency effects, we incorporate sensitivity kernels at the phase velocity inversion stage.

1.2. Sensitivity kernels

In order to account for the finite frequency effects, earlier versions of TPWT implement Gaussian kernels. These kernels do not accurately represent finite frequency effects as they assume a constant Gaussian-shaped sensitivity function perpendicular to the ray path [*Forsyth*, 1998]. On the other hand, modified versions of TPWT use single scattering (Born) approximation sensitivity kernels [*Yang and Forsyth*, 2006a; b] of *Zhou et al.* [2004] (Figure 1.3). 2D sensitivity kernels for fundamental mode surface waves using Born approximation can be described as [*Zhou et al.*, 2004]:

$$K(r,\omega) = \frac{2k^2 S'R'' \exp\{-i[k(\Delta' + \Delta'' - \Delta) - \pi/2\,(n' + n'' - n) + \pi/4]\}}{SR\sqrt{8\pi k \left(\frac{|sin\Delta'||sin\Delta''|}{|sin\Delta|}\right)}} \tag{1.3}$$

where K is the sensitivity kernel as a function of propagation direction (r) and angular frequency (ω). Single and double primed symbols denote waves from source to scatterer, and from scatterer to receiver, respectively. Symbols with no primes indicate direct waves from source to station. The integer n is polar passage index, indicating how many times a wave train passes thorough the source or its antipode. Δ shows the distance between source-scatterer (Δ'), scatterer-receiver(Δ''), or source-receiver(Δ) . Source and receiver polarization terms are indicated using *S* and *R*, respectively.

Real and imaginary parts of Equation (1.3) give amplitude and phase kernels, respectively. These are:

$$K_\phi(r, \omega) = Im\{K(r, \omega)\} \tag{1.4}$$

$$K_A(r, \omega) = -Re\{K(r, \omega)\} \tag{1.5}$$

In the above equations, scattered and direct arriving waves are due to the same earthquake. Therefore, source terms ($S \, and \, S'$) can be neglected. In our case, surface wave tomography is a minor arc problem. Therefore, a wave train never passes through source or its antipode again. Hence, polar passage index is zero (n = 0), and vanishes from the Equation (1.3). Moreover, in the case of Rayleigh waves, only vertical components of seismograms are used. For this reason, receiver polarization vectors (R) for direct and scattered waves are equal [*Yang and Forsyth*, 2006b]. However, Love wave energy is concentrated on the transverse plane; and polarization terms are functions of scattering angle [*Snieder*, 1986].

In reality, sensitivity kernels are not the same for the whole earth. Rather, they are functions of earth structure and may change along the propagation path in their amplitudes and geometry. However, in regional tomography studies, research areas are relatively small. Most probably, variations in sensitivity kernels have a minor role in tomography results, and therefore I make a final assumption and neglect these variations.

1.3. Seismic anisotropy and TPWT

Thus far, I have considered the forward problem of TPWT for an isotropic earth. However, in reality, earth is not isotropic, i.e. seismic wave speeds may change depending on the propagation direction. Seismic anisotropy is a very valuable tool as it is a proxy for the direction of finite strain, i.e. deformation. Sources of seismic anisotropy are not yet clear. Since olivine is the most common mineral in earth's mantle, LPO (Lattice Preferred Orientation) of olivine is thought to be the main cause of anisotropy [*Babuška and Cara*, 1991]. On the other hand, at crustal depths, SPO (Shape Preferred Orientation) of mica and quartz are the most probable cause for anisotropy [*Ward et al.*, 2012].

When employing TPWT, it is possible to measure two types of anisotropy: azimuthal and radial. Azimuthal anisotropy considers the direction in which waves propagate faster, showing the horizontal component of maximum finite strain directions. TPWT solves for azimuthal anisotropy simultaneously with phase wave speeds, using a similar approach to body wave tomography [*Smith and Dahlen*, 1973]. The relationship between the azimuthal fast direction and phase wave speed can be expressed by:

$$C(\omega, \theta) = C_0(\omega) + A(\omega)\cos(2\theta) + B(\omega)\sin(2\theta) \qquad (1.6)$$
$$+ D(\omega)\sin(4\theta) + E(\omega)\sin(4\theta)$$

In Equation (1.6), C is the anisotropic phase velocity as a function of angular frequency (ω) and seismic fast direction (θ). For Rayleigh waves, the 4θ terms in Equation (1.6)

are negligible [*Montagner and Nataf*, 1986]. Therefore, for each frequency, seismic fast direction can be expressed as:

$$2\theta = tan^{-1}\left(\frac{B(\omega)}{A(\omega)}\right) + k\pi \tag{1.7}$$

where k is an integer. Hence, the solution for azimuthal fast direction can be expressed by one of the two orthogonal terms:

$$\theta = \frac{1}{2}tan^{-1}\left(\frac{B(\omega)}{A(\omega)}\right) \ or \ \theta = \frac{1}{2}tan^{-1}\left(\frac{B(\omega)}{A(\omega)}\right) + \frac{\pi}{2} \tag{1.8}$$

The most important limitation of solving for azimuthal anisotropy using above approach includes the trade-off between lateral heterogeneities and anisotropic phase wave speeds. Moreover, TPWT can only solve for average seismic fast directions in pre-defined regions. The advantage of using surface waves to solve azimuthal anisotropy lies in their dispersive characteristics. Each period corresponds to different peak depth sensitivity; hence it is possible to resolve average anisotropy at a depth range. Therefore, surface wave provide depth constraints for measured azimuthal fast directions.

Radial anisotropy is more straightforward. It indicates the direction of deformation in the vertical plane, using the difference between isotropic horizontally (SH) and vertically (SV) polarized shear wave speeds. The most common formulation of radial anisotropy uses variations from the mean wave speed, as expressed by Equation (1.9):

$$2(V_{SH} - V_{SV})/(V_{SH} + V_{SV}). \hspace{3cm} (1.9)$$

1.4. Summary

In this chapter, I have discussed advantages of TPWT over traditional approaches. In addition, I have provided information on the method including forward problem, sensitivity kernels, and seismic anisotropy. Traditional surface wave tomography method uses ray path theory to infer phase or group wave speeds of surface waves, assuming surface waves have infinite frequencies. This assumption limits data and resolution for this approach. TPWT does not share these limitations, as it assumes that distortion of a wavefront can be expressed as the sum of two plane waves. The effects of having finite frequencies are successfully accounted for by employing two-dimensional Born sensitivity kernels. As I show in Chapter 3, TPWT can image anomalies much smaller than the dominant wavelength. Finally, using TPWT, it is also possible to simultaneously solve for azimuthal anisotropy to infer the direction of maximum finite strain.

1.5. References

Argand, E. (1924), La tectonique de l' Asie, paper presented at Proc. 13th Int. Geol. Cong. 7.

Babuška, V., and M. Cara (1991), *Seismic anistropy in the Earth*, 217 pp., Kluwer Academic Publishers, Netherlands.

Barazangi, M., and J. Ni (1982), Veolocities and propagation characteristic of Pn and Sn beneath the Himalayan arc and Tibetan plateau: Possible evidence for underthrusting of Indian continental lithosphere beneath Tibet, *Geology*, *10*, 179-185.

Ceylan, S., J. Ni, J. Y. Chen, Q. Zhang, F. Tilmann, and E. Sandvol (2012), Fragmented Indian plate and vertically coherent deformation beneath eastern Tibet, *Journal of Geophysical Research*, *117*(B11), doi:10.1029/2012jb009210.

Forsyth, D. W. (1998), Phase Velocities of Rayleigh Waves in the MELT Experiment on the East Pacific Rise, *Science*, *280*(5367), 1235-1238, doi:10.1126/science.280.5367.1235.

Forsyth, D. W., and A. Li (2005), Array Analysis of Two-Dimensional Variations in Surface Wave Phase Velocity and Azimuthal Anisotropy in the Presence of Multipathing Interference, in *Seismic Earth: Array Analysis of Broadband Seismograms*, edited by A. L. a. G. Nolet, AGU, Washington DC.

Kind, R., et al. (2002), Seismic images of crust and upper mantle beneath Tibet: evidence for Eurasian plate subduction, *Science*, *298*(5596), 1219-1221, doi:10.1126/science.1078115.

Knopoff, L. (1972), Observation and inversion of surface-wave dispersion, *Tectonophysics*, *13*(1-4), 497-519, doi:http://dx.doi.org/10.1016/0040-1951(72)90035-2.

Li, A. (2011), Shear wave model of southern Africa from regional Rayleigh wave tomography with 2-D sensitivity kernels, *Geophysical Journal International*, *185*(2), 832-844, doi:10.1111/j.1365-246X.2011.04971.x.

Li, L., and A. Li (2012), Radial anisotropy in the northeastern Tibetan Plateau from surface wave tomography, in *AGU Fall Meeting*, edited, San Francisco.

Montagner, J.-P., and H.-C. Nataf (1986), A simple method for inverting the azimuthal anisotropy of surface waves, *Journal of Geophysical Research: Solid Earth*, *91*(B1), 511-520, doi:10.1029/JB091iB01p00511.

Saito, M. (1988), *DISPER80: A subroutine package for the calculation of seismic normal-mode solutions*, Elsevier, New York.

Smith, M. L., and F. A. Dahlen (1973), The azimuthal dependence of Love and Rayleigh wave propagation in a slightly anisotropic medium, *Journal of Geophysical Research*, *78*(17), 3321-3333, doi:10.1029/JB078i017p03321.

Snieder, R. (1986), 3D Linearized scattering of surface waves and a formalism for surface wave holography, *Geophys. J. R. astron. Soc.*, *84*, 581-605.

Sol, S., et al. (2007), Geodynamics of the southeastern Tibetan Plateau from seismic anisotropy and geodesy, *Geology*, *35*(6), 563, doi:10.1130/g23408a.1.

Styron, R., M. Taylor, and K. Okoronkwo (2010), Database of active structures from the Indo-Asian collision, *EOS Trans., AGU*, *91*(20), 181-182, doi:10.1029/2010EO200001.

Tilmann, F., et al. (2003), Seismic Imaging of the Downwelling Indian Lithosphere Beneath Central Tibet, *Science*, *300*(5624), 1424-1427.

Ward, D., K. Mahan, and V. Schulte-Pelkum (2012), Roles of quartz and mica in seismic anisotropy of mylonites, *Geophysical Journal International*, *190*(2), 1123-1134, doi:10.1111/j.1365-246X.2012.05528.x.

Yang, Y., and D. W. Forsyth (2006a), Rayleigh wave phase velocities, small-scale convection, and azimuthal anisotropy beneath southern California, *Journal of Geophysical Research*, *111*(B7), doi:10.1029/2005jb004180.

Yang, Y., and D. W. Forsyth (2006b), Regional tomographic inversion of the amplitude and phase of Rayleigh waves with 2-D sensitivity kernels, *Geophys. J. Int.*(166), 1148-1160.

Yue, H., et al. (2012), Lithospheric and upper mantle structure of the northeastern Tibetan Plateau, *J. Geophys. Res.*, *117*(B5), B05307, doi:10.1029/2011jb008545.

Zhao, W., et al. (2011), Tibetan plate overriding the Asian plate in central and northern Tibet, *Nature Geosci*, *4*(12), 870-873, doi:10.1038/NGEO1309.

Zhou, H., and M. Murphy (2005), Tomographic evidence for wholesale underthrusting of India beneath the entire Tibetan plateau, *Journal of Asian Earth Sciences*, *25*(3), 445-457, doi:10.1016/j.jseaes.2004.04.007.

Zhou, Y., F. A. Dahlen, and G. Nolet (2004), Three-dimensional sensitivity kernels for surface wave observables, *Geophysical Journal International*, *158*(1), 142-168, doi:10.1111/j.1365-246X.2004.02324.x.

Chapter 2: Fragmented Indian Plate and vertically coherent deformation beneath E. Tibet[1]

Abstract

Using fundamental mode Rayleigh waves from the INDEPTH-IV and Namche-Barwa seismic experiments for periods between 20-143 s, I have investigated the lithospheric structure beneath eastern Tibet. I have found a ~200-km-wide high velocity body, starting at ~60 km depth and roughly centered beneath the Bangong-Nijuang Suture, which is most likely a piece of the underthrusting Indian continental lithosphere. The sub-horizontal underthrusting of the Indian lithosphere beneath eastern Tibet appears to be accompanied by its lateral tearing into at least two fragments, and subsequent break-off of the westernmost portion at ~91°E-33°N. The uppermost mantle low velocity zone I observe beneath the N. Qiangtang and Songpan-Ganzi terranes is most probably due to warmer and thinner lithosphere relative to southern Tibet. I attribute the low velocity zones concentrated along the northern and southern branches of the eastern Kunlun fault at lithospheric depths to strain heating caused by shearing. The azimuthal

---

[1] Original article: Ceylan, S., J. Ni, J. Y. Chen, Q. Zhang, F. Tilmann, and E. Sandvol (2012), Fragmented Indian plate and vertically coherent deformation beneath eastern Tibet, J. Geophys. Res., 117, B11303, doi:10.1029/2012JB009210.

fast directions at all periods up to 143 s (~200 km peak sensitivity depth) beneath the N. Qiangtang and Songpan-Ganzi terranes are consistent, suggesting vertically coherent deformation between crust and uppermost mantle. Furthermore, the low velocity zone below the Kunlun Shan reaching down to >200 km argues against a present southward continental subduction along the southern margin of Qaidam Basin.

2.1. Introduction

Collision between the Indian and Eurasian plates ~50 Ma [*Argand*, 1924; *Molnar and Tapponnier*, 1975; *Yin and Harrison*, 2000] has led to the formation of the world's largest and highest continental landform: the Tibetan Plateau. Despite numerous studies over the last two decades, the dominant mechanism for the deformation and uplift of the Tibetan Plateau is still being debated. The growth and dynamics of this highly studied, yet poorly understood continental collision are commonly attributed to four different but not necessarily mutually exclusive geodynamic models: escape tectonics along major strike-slip faults and southward continental subduction [*Tapponnier et al.*, 2001], wholesale underthrusting of the Indian plate [*Argand*, 1924; *Ni and Barazangi*, 1984; *Zhou and Murphy*, 2005], ductile flow at mid- to lower crustal depths [*Clark et al.*, 2005; *Clark and Royden*, 2000], and coherent deformation between the crust and lithospheric mantle [*Bendick and Flesch*, 2007; *Silver*, 1996].

Evidence from gravity [*Jimenez-munt et al.*, 2008], body wave tomography [*Tilmann et al.*, 2003; *Zhou and Murphy*, 2005], Pn velocity [*Liang and Song*, 2006; *McNamara et al.*, 1997], shear wave splitting [*Chen et al.*, 2010; *Huang et al.*, 2000], and receiver function [*Kind et al.*, 2002] studies strongly suggests that southern Tibet is

underlain by relatively colder, more rigid Indian continental lithosphere, possibly

extending past the Bangong-Nijuang Suture (BNS; see Figure 2.1).
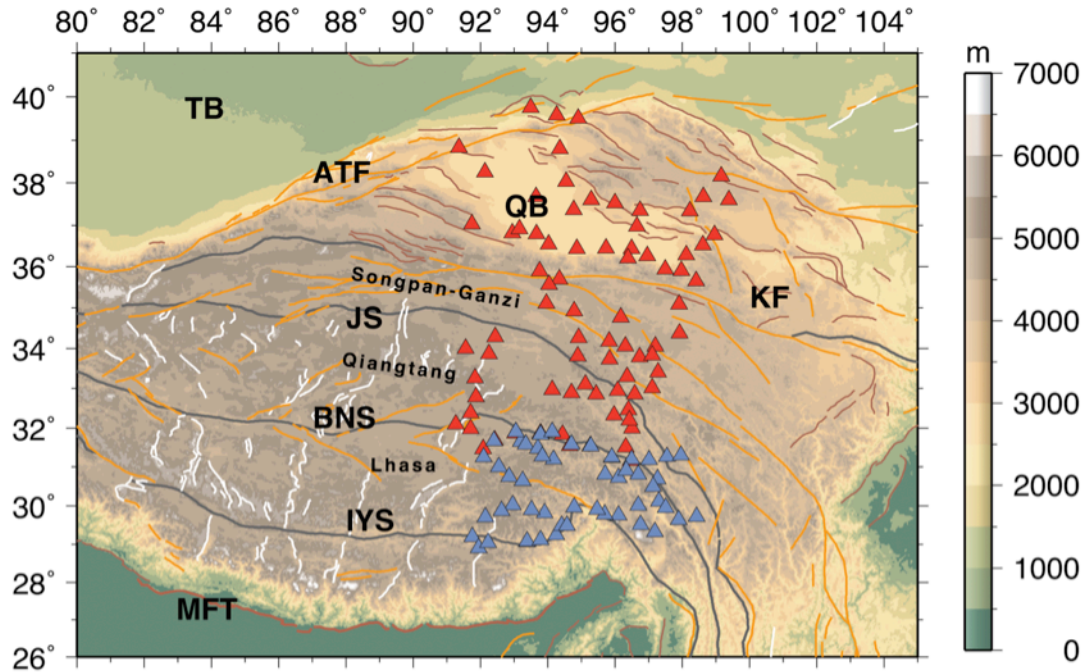
Figure 2.1. Seismic station locations (red triangles are INDEPTH-IV stations, blue triangles indicate Namche-Barwa stations) with tectonic features [*Styron et al.*, 2010]. White and brown lines show normal and thrust faults, respectively. Orange lines represent strike-slip faults. Suture zones are marked by thick gray lines. IYS: Indus-Yarlung suture; BNS: Bangong-Nujiang Suture; JS: Jinsha Suture; KF: Kunlun Fault; QB: Qaidam Basin; TB: Tarim Basin; ATF: Altyn-Tagh Fault; and MFT: Main Frontal Thrust.

Images obtained by P-to-S conversions along a NS trending profile at ~85°E [*Nabelek et*

al., 2009] show indications of Indian lower crust beneath Tibet beyond the Indus-Yarlung

suture (IYS) to ~31°N. Another P-to-S conversion study by *Kosarev et al.* [1999]

presents evidence for northward dipping Indian lithosphere beneath southern Tibet.

Similarly, P-wave tomography results from INDEPTH-III (InterNational DEep Profiling

of Tibet and the Himalayas) seismic experiment [*Tilmann et al.*, 2003] reveal a sub-vertically downwelling high velocity body beneath BNS interpreted as a part of the underthrusting Indian continental lithosphere (UICL). S-to-P conversion [*Kumar et al.*, 2006; *Zhao et al.*, 2010] and body wave tomography [*Li et al.*, 2008; *Liang et al.*, 2012] studies demonstrate that the E-W geometry and thickness of the underthrusting Indian plate is significantly variable. Further north, slow Pn and inefficient Sn waves north of the BNS are interpreted as warmer uppermost mantle [*Barazangi and Ni*, 1982; *Ni and Barazangi*, 1984]. In contrast to these observations and in support of the wholesale underthrusting/subduction model, global body wave tomography images [*Zhou and Murphy*, 2005] and some continent-scale surface wave models [*Priestley et al.*, 2006] show fast upper mantle velocities beneath most of Tibet, suggesting that the UICL has subducted sub-horizontally beneath the entire plateau to depths of ~200 km, and has a variable lateral geometry and dip. Additionally, P [*Kind et al.*, 2002] and S [*Zhao et al.*, 2011] receiver function images show an apparent southward continental subduction south of the Qaidam Basin.

Due to insufficient coverage of existing seismic experiments in the Plateau, the nature and northward extent of the subducted Indian plate, and structure beneath the Plateau are not well known. Additionally, a comparison of previous surface and body wave tomography results [*Li et al.*, 2008] shows significant discrepancies beneath southeastern Tibet. Here, in order to further constrain the dominant deformational mechanisms within the Plateau and the geometry of the UICL, I present a new Rayleigh wave tomography model based on the INDEPTH-IV and Namche-Barwa [*Sol et al.*, 2007] experiments (Figure 2.1) in north-central and southeastern Tibet, respectively. I

address the following: (1) what is the northward extent of the UICL and what is its geometry, (2) is there southward continental subduction south of the Qaidam Basin, and (3) what is the horizontal finite strain fabric beneath eastern Tibet and is there evidence for vertically coherent deformation?

2.2. Data and methods

I use fundamental mode Rayleigh waves and two-plane wave tomography (TPWT) for phase velocity inversions [*Forsyth and Li*, 2005]. I choose earthquakes with epicentral distances between 20° and 120°, depth ≤ 100 km, and M_S ≥ 5.7. I only use the vertical component in order to avoid shear and Love wave interference, and long period noise that may exist on horizontal components. The events with low signal to noise (S/N) ratios are eliminated visually. My data was recorded from INDEPTH-IV array (74 broadband stations) that was deployed across Northern Tibet (Figure 2.1). I have also included data from the Namche-Barwa seismic array [*Sol et al.*, 2007] in southeastern Tibet. Prior to data processing, all instrument responses are converted to the first generation STS2. I measure phase velocities for 13 frequency bands ranging between 20 and 143 s, and utilize 10-mHz-wide Butterworth filters centered on each frequency. In order to avoid dependence on earthquake magnitude, I normalize the seismic wave amplitude for each event, then measure phases and amplitudes of visually windowed data using Fourier analysis. I have used a total of 174 earthquakes. In order to increase the reliability of my inversions, I only include events that were recorded by at least 10 stations.
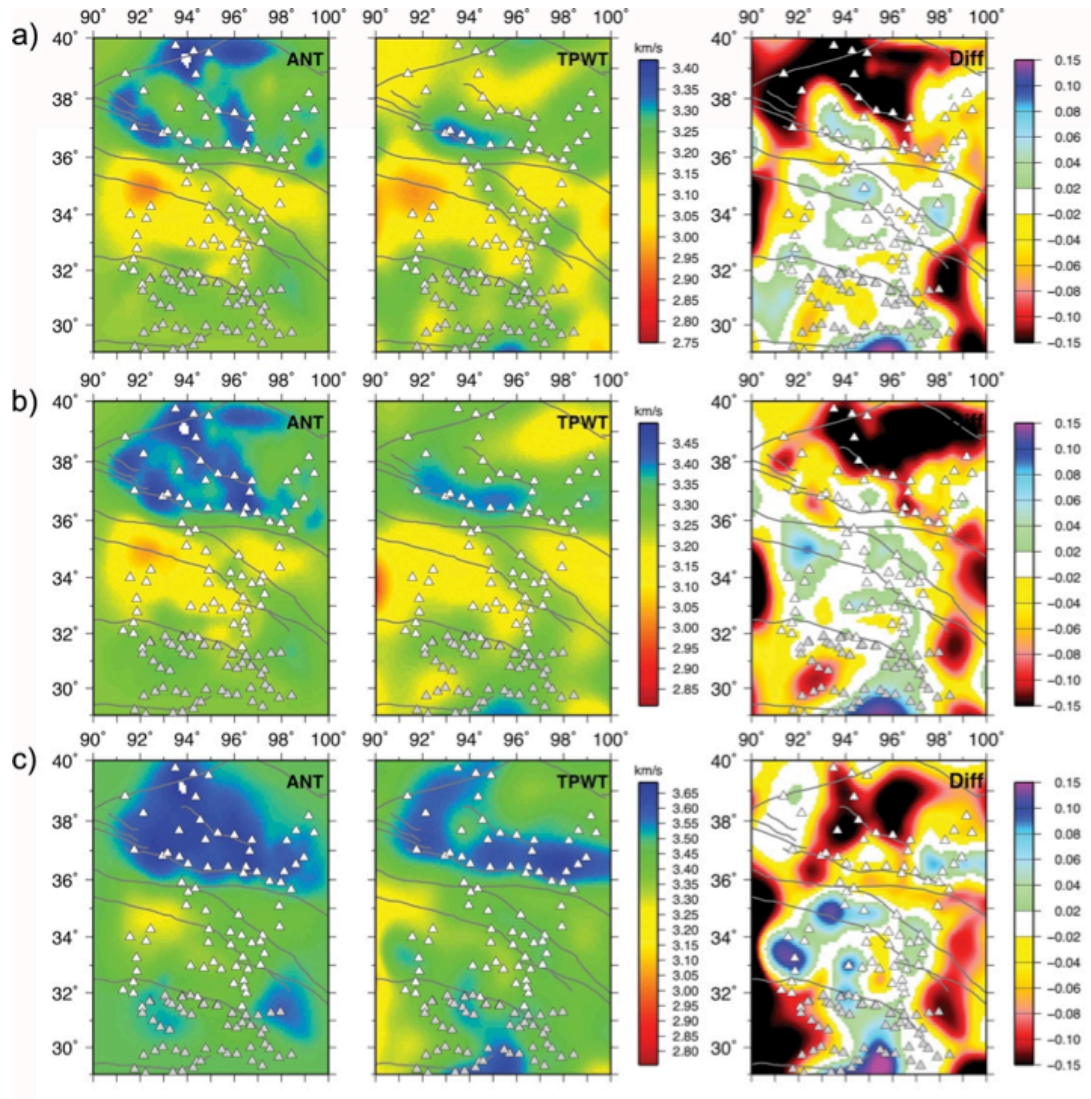
Figure 2.2. The difference between isotropic phase velocities obtained using ambient noise tomography (ANT) [*Yang et al.*, 2010] and two-plane wave approach (TWPT) for periods of a) 25, b) 30, and c) 40 s. The third column shows the difference between two methods in km/s. These results show that within the seismic array (with the exception of Qaidam Basin), phase velocities obtained by two methods are similar (~±0.06 km/s).

The first step in my inversions is calculating isotropic phase velocities for each frequency. My experiments with TPWT show that ~60 events are enough to obtain stable results. However, in order to better constrain the inversion parameters (i.e. smoothing length and damping), I compare my results with those of Ambient Noise Tomography

(ANT) [*Yang et al.*, 2010]. Although both methods measure surface wave dispersion, ANT and TPWT are fundamentally different and use independent data sets: TPWT implements surface waves created by earthquakes while ANT excludes earthquakes and uses ambient noise of the earth. Additionally, while ANT uses ray theory to obtain phase maps, TPWT assumes that distortion of wavefronts at each station can be expressed as the sum of two plane waves [*Forsyth and Li*, 2005]. Due to the short wavelengths of ambient surface waves, ANT can typically obtain more reliable results at crustal depths than TPWT. There is an overlapping frequency range between these two methods (in this case 20-50 s).

The comparison of isotropic phase velocities indicates that within the seismic array, these two methods reveal very similar results (differences less than ± 0.06 km/s with the exception of Qaidam Basin) for periods between 25 and 40 s (Figure 2.2). With the exception of 125 s (~170 km), the checkerboard tests (Figure 2.3) imply that resolution within the seismic array is ~150 km or better at all periods, sufficient to image all of the anomalies discussed in this study. However, due to insufficient ray paths from the W-NW (auxiliary material Figure 2.1), the checkerboard tests exhibit evidence for some lateral smearing.

The second step of phase velocity inversion includes determining anisotropic phase velocities and seismic fast directions (Figure 2.4). Unlike traditional ray theory, TPWT accounts for phase and amplitude changes. A disadvantage of this method is its sensitivity to finite frequency effects such as scattering and wave front healing [*Hung et al.*, 2001; *Nolet and Dahlen*, 2000]. To overcome these limitations, I employ 2D sensitivity kernels [*Yang and Forsyth*, 2006] for both amplitude and phase perturbation

21

for each period. Azimuthal anisotropy is simultaneously solved with Rayleigh wave phase velocities. Since the shortest wavelength for data I use is ~65 km (for 20 s period and taking average phase velocity as 3.18 km/s), I use a constant smoothing length of 80 km for all periods. There is always a trade off between lateral heterogeneity of
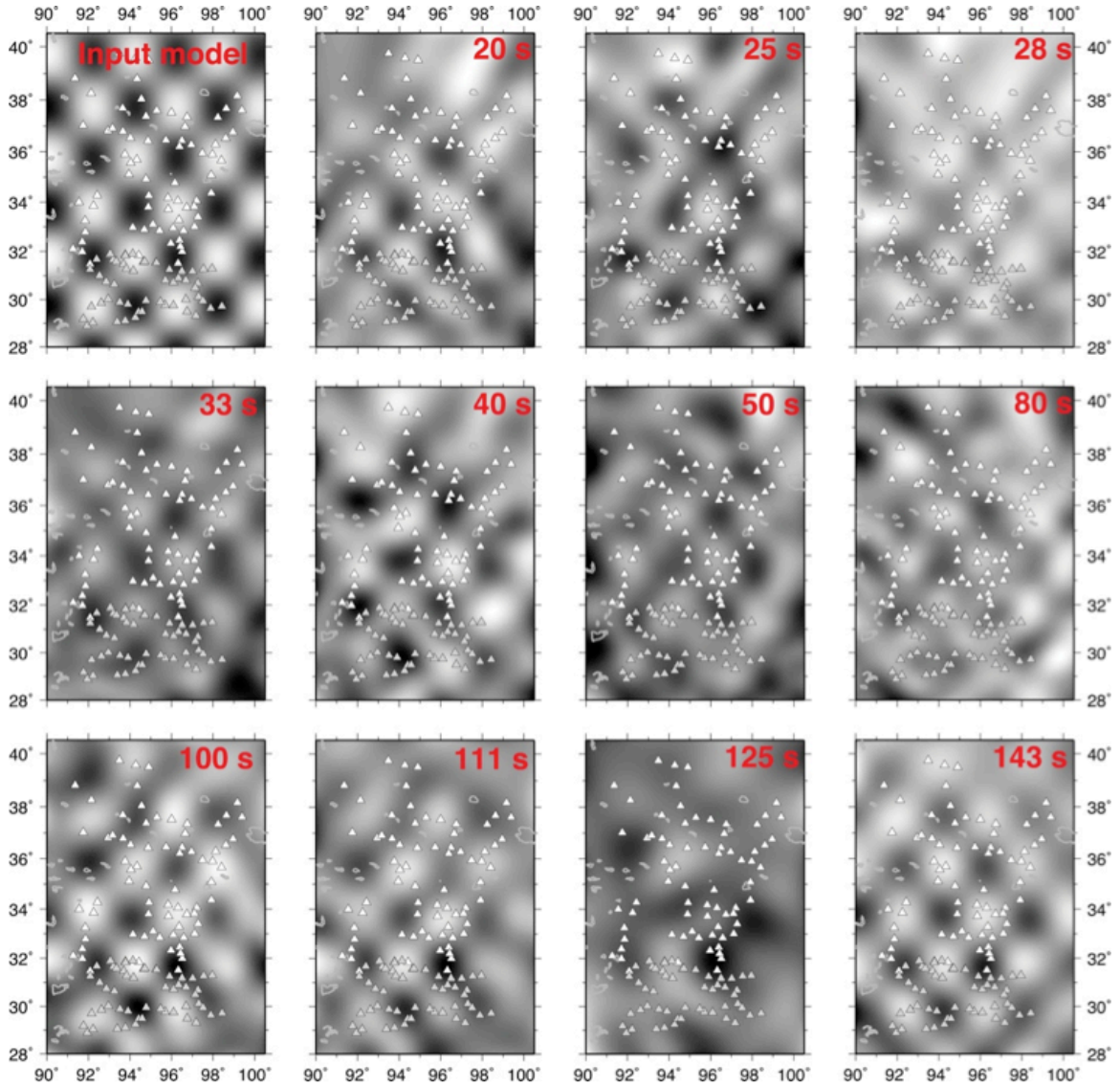
Figure 2.3. The resolution test results for different periods using checkerboard synthetic model. The anomalies in the input model are 1.5°x1.5°. The periods are indicated upper-right corner of each panel.
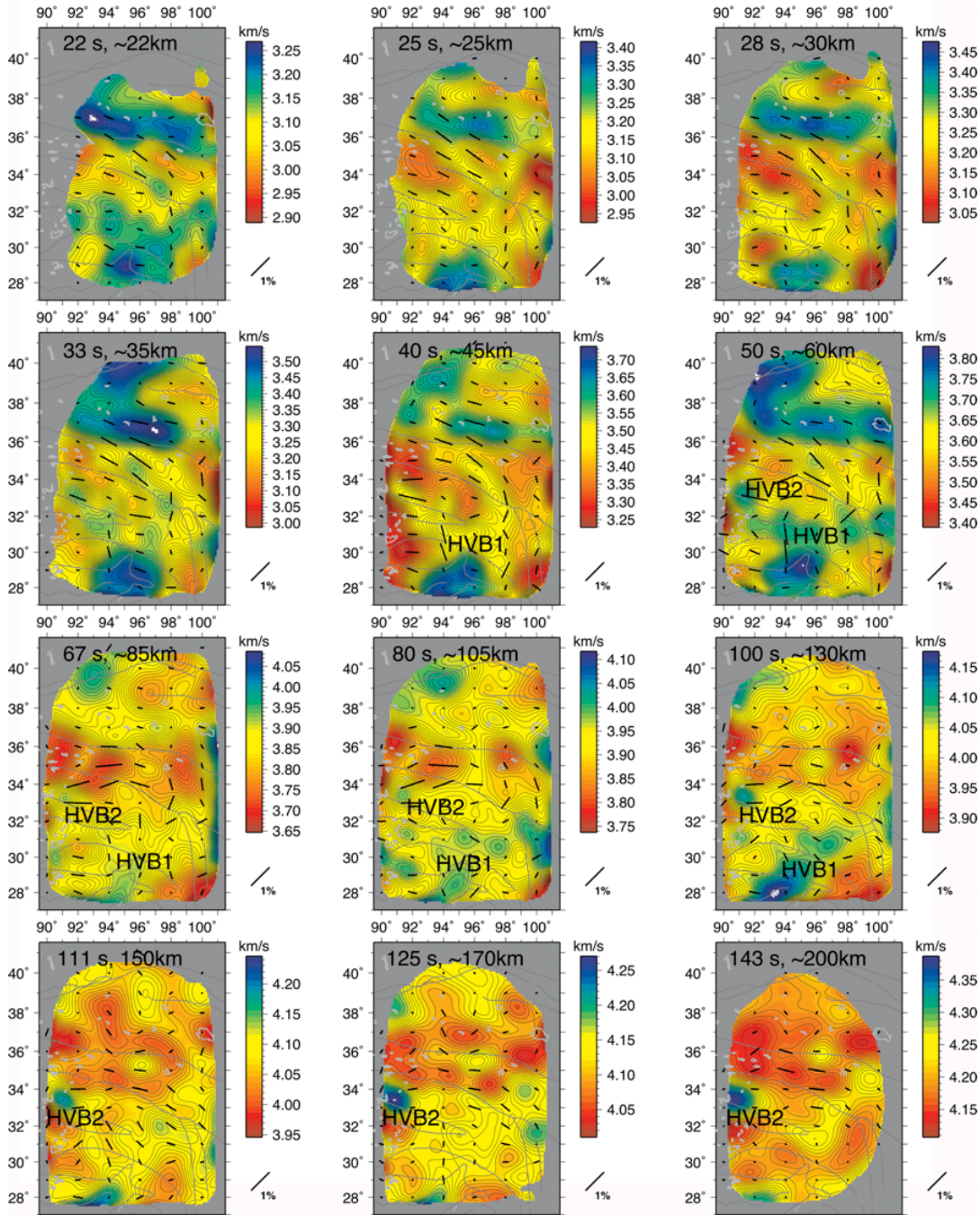
Figure 2.4. Anisotropic phase velocity maps for 12 periods (22-143 s). The solid black lines indicate azimuthal fast direction and amplitude of anisotropy. Note that color scales are different for each map. The regions with errors of $2\sigma \leq 0.06$ km/s (where σ is the standard deviation) are shaded. HVB1 and HVB2 show the high velocity bodies addressed in the text.
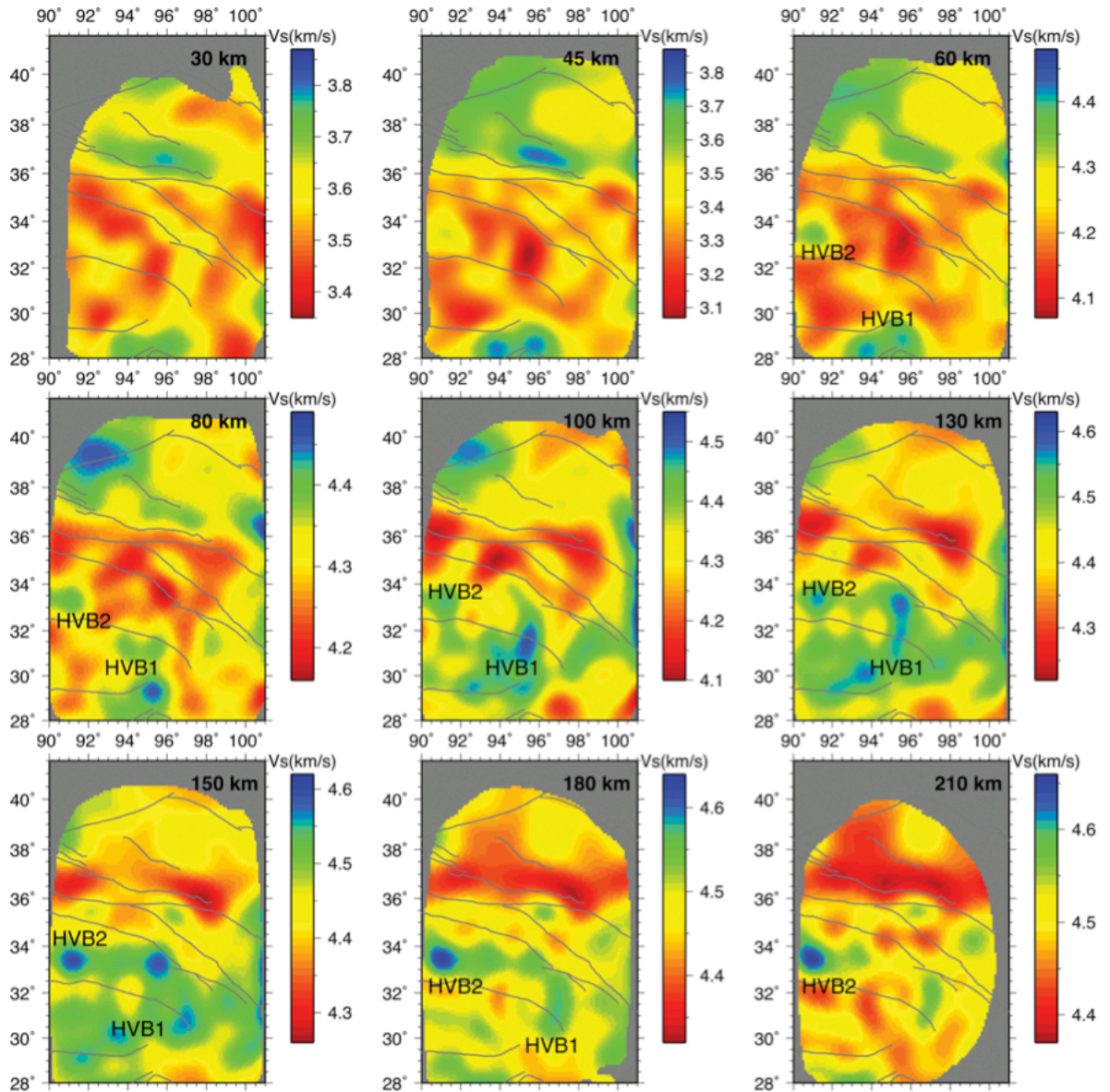
Figure 2.5. Shear wave velocities (km/s) for depths between 30 and 210 km. Depths are indicated on each panel. Note that each panel has a different color scale. The dark gray lines show major tectonic features. HVB1 and HVB2 are the same as referenced to in the text. The regions with errors of $2\sigma \leq 0.06$ km/s (where σ is the standard deviation) are shaded, based on peak depth sensitivity of corresponding frequencies. An unmasked version of this image is provided in auxiliary material Figure 2.6.

isotropic phase maps and anisotropy. In order to reduce the effects of this trade-off, I use high damping both for anisotropy and phase velocities. Additionally, I have tested my inversion results by using a variety of damping values. However, the final choice of damping parameter was made considering model uncertainties (auxiliary Figure 2.2) and consistency with ANT results. Moreover, the features I discuss here are consistently observed in all inversions regardless of damping. Additionally, to increase reliability, I only interpret phase velocities with errors $2\sigma \le 0.06$ km/s, where σ is the standard deviation.

The third and last step of the inversion is obtaining shear wave velocities (Figures 2.5 and 2.6) using the anisotropic phase maps from the second step. For shear wave inversions, I use the partial derivatives from *Saito* [1988]. For the initial model, the AK135 model is adapted to my region by taking average Moho depths of 45 and 60 km for Qaidam Basin and the rest of the region [*Zhu and Helmberger*, 1998], respectively.

I defined 50 layers for shear wave inversion from the surface to 400 km depth. According to *Li* [2011], who used a similar frequency range with less data, the shear wave structure cannot be determined precisely at all layers, but the average velocity for each defined layer can be resolved for depths less than 250 km. Therefore, I do not interpret my results for depths > 200 km.

2.3. Results

Figures 2.4-2.6 show my tomographic models for Rayleigh wave phase and shear wave velocities. Starting from the south, I observe a high velocity body (HVB1) along the BNS and further south, between the depths of ~60 and 170 km. This feature is highly

heterogeneous in the east-west direction with a shear wave anomaly of ≥ 2%.

Furthermore, the phase velocity maps (Figure 2.4) show regions of relatively low

velocities within the HVB1. The shear wave anomaly cross-sections (Figure 2.6)

demonstrate that the HVB1 has a sub-horizontal geometry dipping northwards slightly

beneath the BNS, between ~94°E and 97°E. A further isolated high velocity body

(HVB2) is observed at ~91°E-33°N which appears to be connected to the HVB1 beneath

the BNS at ~130-150 km, becoming isolated again at greater depths. This vertically

continuous feature starts at ~60 km depth (50 s) and gradually increases in diameter to

depths greater than 200 km (Figures 2.4 and 2.5).

Further north, low velocities characterize the uppermost mantle beneath the N.

Qiangtang and Songpan-Ganzi. The shear wave velocities are ~4% slower than those

observed beneath the Lhasa block and southern Qiangtang terrane (Figure 2.5).

Anisotropic fast directions (Figure 2.4) across the northern and southern branches of the

Kunlun Fault tend to conform to strikes of the active faults (±15°). I also observe the

largest amplitude of azimuthal anisotropy across these shear zones. Seismic anisotropy

appears to be consistent at depth (± 15°) with the exception of the southeast portion of my

study region. Similar to shear wave splitting measurements [*Huang et al.*, 2000; *León*

Soto et al., 2012], azimuthal fast directions exhibit a general clockwise rotation (auxiliary

Figures 2.3 and 2.5).
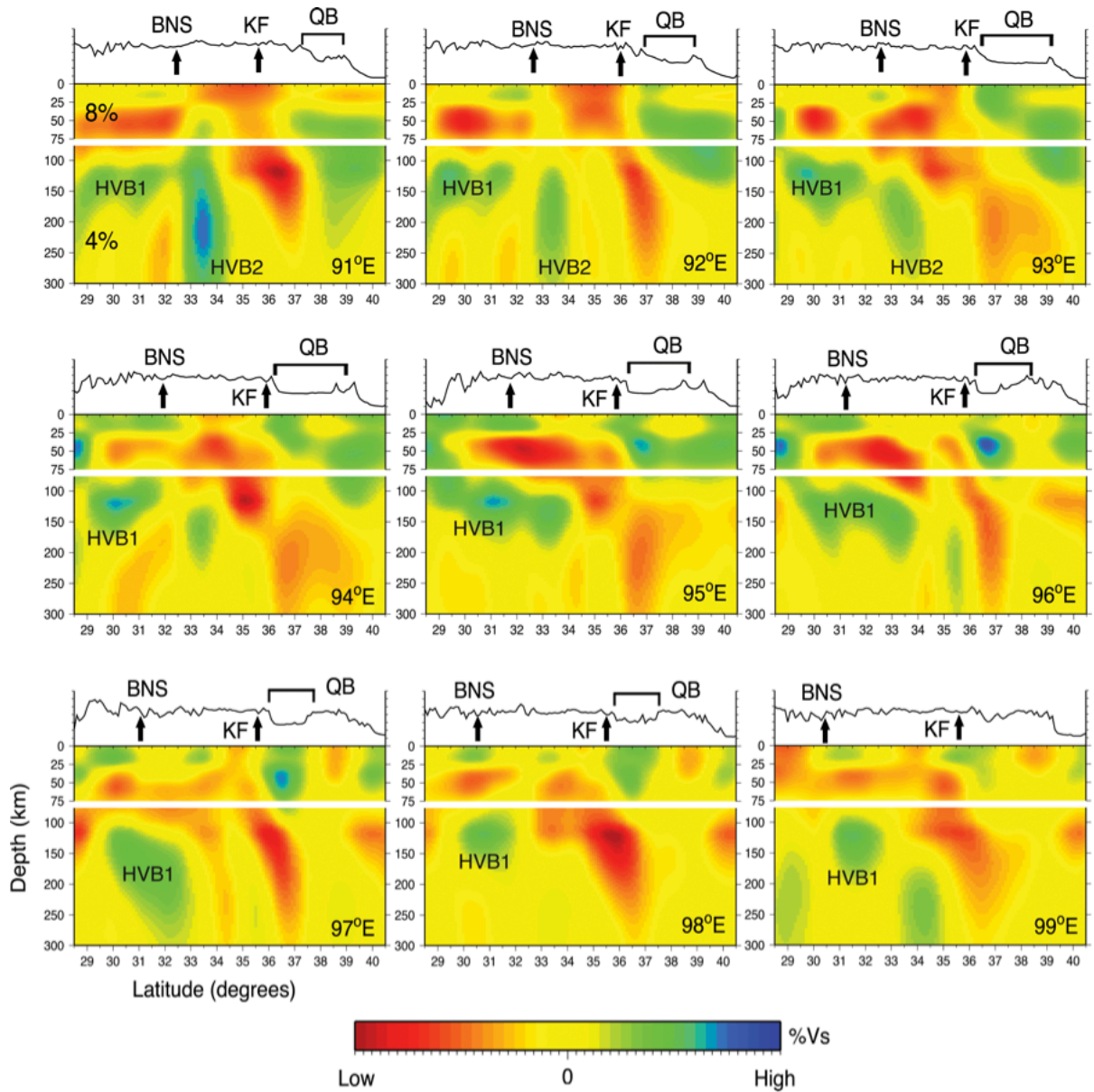
**Figure 2.6.** Shear wave (SV) anomalies along 91°E-99°E. 0-75 km and 75-300 km depth ranges were colored using 8% and 4% variation according to the mean value at each depth, respectively. Major structures are marked on the topography profiles for each profile. For additional profiles see supplementary materials. HVB1 and HVB2 indicate the high velocity bodies discussed in the text. Other abbreviations are the same as Figure 2.1.

Both phase maps and S wave anomalies (Figure 2.6) show ~1% higher velocities, indicating thicker (~130-140 km) and possibly rigid lithosphere beneath the Qaidam Basin. I also observe the eastern edge of the Tarim Basin (auxiliary Figure 2.4). In an approximate agreement with the lithosphere-asthenosphere boundary (LAB) phases of S-wave receiver functions [*Zhao et al.*, 2011], the Tarim Basin has a lithospheric thickness of ~200 km, while the Qaidam Basin is substantially thinner. Beneath the Kunlun Shan, south of Qaidam Basin, I observe low velocity zones that are concentrated along the northern and southern branches of the Kunlun Fault, extending deeper than 200 km.

Comparisons with independent phase maps using ambient noise [*Yang et al.*, 2010] suggest that I am able to measure the phase velocities with a high degree of precision (differences less than 0.06 km/s within the array, Figure 2.2). Furthermore, unlike previous surface and body wave measurements [*Li et al.*, 2008], my shear wave observations are broadly consistent with those obtained using body wave tomography [*Liang et al.*, 2012]. Moreover, the comparison of the splitting data from *León Soto et al.* [2012] and my azimuthal fast directions for 143 s shows that average differences are ~14° and 10° for Qiangtang and Songpan-Ganzi, respectively (auxiliary Figure 2.5).

2.4. Discussion

2.4.1. High velocity body beneath Lhasa and southern Qiangtang terrane

Presuming that the Indian plate does not extend substantially past the BNS, the high velocity body (HVB1) in my images beneath the BNS could be explained by large-scale delamination of the Eurasian plate. However, considering the compelling evidence

28

for the continuation of Indian plate into the central part of the Plateau [*Kind et al.*, 2002; *Nelson et al.*, 1996; *Tilmann et al.*, 2003] as well as the lack of recent volcanism, a delamination model is not well supported. My results reveal a low velocity zone north of the BNS at depths of ~90-200 km, indicating a thinner and possibly warmer lithosphere beneath the northern Qiangtang and Songpan-Ganzi terranes [*Haines*, 2003; *Tilmann et al.*, 2003; *Zhou and Murphy*, 2005]. Along the BNS and further south, both shear wave velocity (Figures 2.5 and 2.6) and Rayleigh wave phase maps (Figure 2.4) indicate the presence of a high velocity body. The compatibility between these observations and those of prior studies strongly suggests that the high velocity zone underlying the BNS represents the Indian continental lithosphere. The heterogeneity of this anomaly argues against a wholesale underthrusting model [*Barazangi and Ni*, 1982] in eastern Tibet. According to the phase and shear wave velocity maps (Figures 2.4 and 2.5), the underthrusting Indian continental lithosphere (UICL) extends from lower crustal depths to ~170 km, and is very heterogeneous in the east-west direction. Because of the slight northward dip of the HVB1, the transition from fast to slow anomalies occurs almost exactly at the BNS and directly below the Moho (~80 km; Figure 2.5), in accordance with the previous Pn velocity [*McNamara et al.*, 1997] and Sn blockage observations [*Barazangi and Ni*, 1982; *Barron and Priestley*, 2009].

Based on my tomographic models (Figures 2.4-2.6), underthrusting is accompanied by lateral fragmentation of the UICL into two wings. The fragmentation initiates at ~30°N-96°E at ~100 km depth. Figure 2.7 shows the proposed geometry of the UICL, using a 2% faster shear-wave anomaly isosurface. I suggest that the oblique collision between India and Eurasia, and oroclinal bending in the EHS may have caused

29

the fragmentation. Flattening of the UICL during sub-horizontal underthrusting may also

have influenced this fragmentation by increasing extensional stresses due to decrease in

the earth's radius.
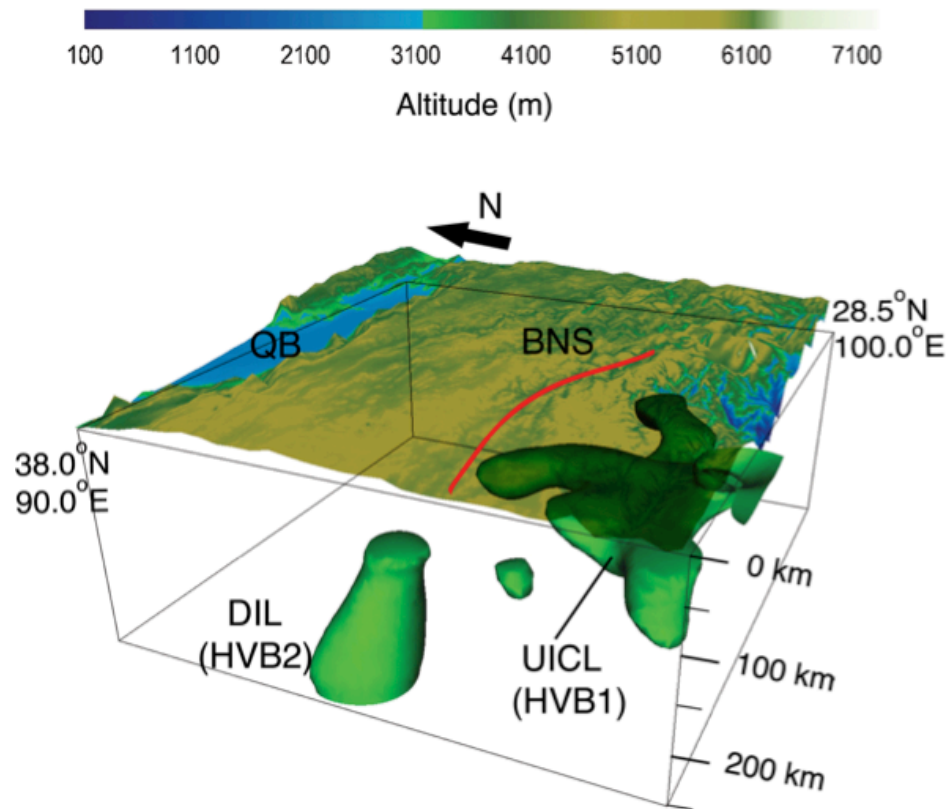
Figure 2.7. Isosurface for 2% faster shear waves for 60 km and deeper, overlain by topography (28.5°-38.0°N and 90.0°-100.0°E). Altitudes are shown by color scale (top). QB: Qaidam Basin; BNS (red line): Bangong-Nujiang Suture; DIL: Detached Indian Lithosphere (referred to as HVB2 in the text); UICL: Underthrusting Indian continental lithosphere (referred to as HVB1 in the text). View from azimuth 245° and tilt 67° from vertical.

Alternatively, this geometry may be a result of chemical heterogeneity within the UICL.

However, my observations of average phase velocities are more consistent with a highly

deformed continental lithosphere rather than a stable shield (e.g. *Chevrot and Zhao*

[2007]). Furthermore, low phase velocities within the UICL are nearly as low as the low

velocities in the north, where there clearly is no UICL.

The second high velocity body (HVB2) I observe is located ~100 km north of the

BNS beneath the Qiangtang Terrane (between ~91°-92°E) and is the strongest anomaly

reaching to depths > 200 km (Figure 2.5). This structure may result from an ongoing

Rayleigh-Taylor instability of the Asian lithosphere. Given that this is the case, both its

vertical position as well as its thermal state can be predicted. The most recent mafic

potassic volcanism (~13 Ma; *Turner et al.* [1996]) in the vicinity of the HVB2 provides

insight into initiation of a possible instability. In order to estimate the vertical position of

the HVB2 in the mantle, I use the mechanical modeling code provided by *Gerya* [2010].

To approximate the thermal state of a cold body residing in the asthenosphere for the

given amount of time, I use the heat conduction equation $\partial T/\partial t + u.\nabla T = \kappa \nabla^2 T$, where κ

is temperature independent thermal diffusivity (10^{-6} m^2/s). The term $u.\nabla T$ represents the

advection term, where u is convergence (or sinking) rate in m/s. I use an ambient

asthenosphere temperature of 1300°C and an initial uniform temperature of 600°C for the

HVB2. For my purposes, I ignore shear and radiogenic heating terms.

Assuming a low mantle viscosity (10^{18} Pas), the HVB2 would be predicted to sink

below depths observable by my method (>250 km). However, supposing a higher mantle

viscosity (10^{21} Pas), the HVB2 would sink at a rate of ~6.0 mm/yr [*Gerya*, 2010]. At this

rate, similar to my observations, the HVB2 would have sunk ~80 km into the

asthenosphere. Using a slow rate of sinking (high viscosity), thermal conductivity

modeling predicts that a delaminated HVB2 would be ~200°C warmer (800°C) at its

center, and consequently have a lower shear wave velocity. However, similar to the Indian lithosphere, the HVB2 has ~4.5% higher velocity than the Songpan-Ganzi, implying that it is colder, more rigid, and may have a different composition. In light of structures with similar S-wave velocities, the observed continuous vertical geometry of the HVB2 (Figures 2.4-2.6), evidence from previous body wave and receiver function studies [*Kind et al.*, 2002; *Kosarev et al.*, 1999; *Tilmann et al.*, 2003], I interpret this body to be the northernmost extent of the UICL, possibly tearing off from the westernmost fragment. Observed both in my results and *Liang et al.* [2012], the HVB2 may be a continuation of the body observed by *Tilmann et al.* [2003] at ~89°E, adjacent to my study region to the west.

2.4.2. Northern Qiangtang and Songpan-Ganzi terranes

Consistent with slow Pn and inefficient Sn propagation observations [*Barazangi and Ni*, 1982; *McNamara et al.*, 1997], the N. Qiangtang and Songpan-Ganzi terranes are underlain by a low-velocity upper mantle. This low velocity anomaly correlates with Late Tertiary basaltic volcanism and has 4-4.2% slower shear-wave velocities (4.3-4.4 km/s at 130 km) than those observed beneath the Lhasa block and southern Qiangtang terrane. The Qiangtang and Songpan-Ganzi have the highest amplitude seismic anisotropy with EW and NW-SE fast directions. Velocity perturbations correspond to a 300°C anomaly [*Wittlinger et al.*, 1996] in the uppermost mantle, which may be due to viscous heating [*Kincaid and Silver*, 1996] or a mantle up-welling associated with small scale convection induced by the underthrusting/subduction of Indian lithosphere [*Tilmann et al.*, 2003].

Alternatively, very localized upwelling caused by strong coupling between the top of the asthenosphere and escaping lithosphere may have resulted in a low velocity mantle lid. However, the observed pattern of low velocities does not fit this model as well as the viscous strain heating model. The pattern of low shear wave velocities correlates well with the active faulting and regions of highest strain rate [*Gan et al.*, 2007]. The absence of a high velocity body below the northernmost plateau argues against models proposing pure shear shortening of Asian lithosphere and/or underthrusting of the UICL beneath the entire plateau.

The general clockwise rotation of seismic fast directions is consistent with shear-wave splitting results [*Huang et al.*, 2000; *León Soto et al.*, 2012]. Fast directions obtained from seismic anisotropy can be used as proxies for the direction of mantle finite strain, resulting from Lattice Preferred Orientation (LPO) of olivine in the upper mantle [*Montagner and Guillot*, 2002]. With the exception of the southeast portion of my region where I lose resolution, the azimuthal fast directions are consistent (± 15°) at all periods, suggesting that the crust and mantle deformation is vertically coherent beneath the N.Qiangtang and Songpan-Ganzi. Furthermore, my observations evince that this coherence extends into the asthenosphere.

2.4.3. Kunlun Fault and Qaidam Basin

My tomographic models show low velocity zones at mid-lower crustal depths, concentrated along the two branches of the Kunlun Fault. Anisotropic fast directions (Figure 2.4) across these shear zones tend to conform to faults' strikes (±15°). This is

33

more apparent at mid-upper crustal depths, indicating that shearing is the dominant deformation mechanism along these zones. Recent strain heating experiments [*Nabelek et al.*, 2010; *Whittington et al.*, 2009] demonstrate that thermal diffusivity decreases much faster with depth than previously thought. An implication of this finding includes that partial melting could be induced by trapped viscous strain heating (produced by non-brittle deformation of mantle material) along major shear zones associated with Tibetan strike-slip faults. This model is consistent with high strain rates [*Gan et al.*, 2007] and the observed low velocity zones that are centered along northern and southern branches of the Kunlun in northern Tibetan Plateau. Moreover, assuming a constant shear stress, as viscosity decreases, strain rate and viscous heating should increase. Alternatively, keeping the strain rate constant and assuming a change in viscosity decreases over time ($\partial\eta/\partial t \rightarrow 0$, where η is viscosity), strain heating becomes constant and causes a temperature anomaly [*Burg and Gerya*, 2005]. In either case, in accordance with my observations (Figure 2.6), it may be plausible that strain heating can extend into the asthenosphere along major shear zones beneath N. Tibet.

In support of the continental subduction model, receiver functions findings [*Kind et al.*, 2002; *Kosarev et al.*, 1999] suggest a south dipping mantle converter beneath the northern margin of the Plateau. However, there is no indication of southward continental subduction or overriding of Tibetan lithosphere [*Zhao et al.*, 2011] in my tomographic models. Instead, I observe a continuous low velocity anomaly up to the Kunlun fault, south of the Qaidam Basin. These boundaries seen in receiver function images, which were interpreted to be indicative of southward continental subduction, might instead represent preserved mantle reflectors [*Yue et al.*, 2012].

2.5. Conclusions

My primary conclusions are as follows:

(1) I observe a high velocity structure beneath the Lhasa and southern Qiangtang down to ~170 km depth, and I interpret this anomaly as the UICL.

(2) The UICL has a sub-horizontal geometry, and tears laterally into at least two fragments beneath southeastern Tibet. The westernmost branch appears to be detached and vertically sinking into the asthenosphere.

(3) The uppermost mantle beneath the N. Qiangtang and Songpan-Ganzi terranes are characterized by low velocities, probably due to warmer lithosphere caused by viscous strain heating or upwelling of the astenosphere. The observed low velocity zones are concentrated along the Kunlun Fault. I attribute this observation to trapped strain heating caused by shearing. Additionally, fast directions across this shear zone tend to conform to active faults' strikes (within the range of ±15°), implying that horizontal shearing is the dominant deformational mechanism.

(4) Azimuthal fast directions beneath the Qiangtang and Songpan-Ganzi terranes are consistent at depth, supporting vertically coherent deformation extending from the crust into the mantle.

(5) My tomographic images outline the Qaidam Basin with ~1% higher anomalies down to depths of ~130 km. The low velocities below the Kunlun range provide evidence against continental subduction along northeastern edge of the Tibetan Plateau.

2.6. Acknowledgements

2.7. References

Argand, E. (1924), La tectonique de l' Asie, paper presented at Proc. 13th Int. Geol. Cong. 7.

Barazangi, M., and J. Ni (1982), Veolocities and propagation characteristic of Pn and Sn beneath the Himalayan arc and Tibetan plateau: Possible evidence for underthrusting of Indian continental lithosphere beneath Tibet, *Geology*, *10*, 179-185.

Barron, J., and K. Priestley (2009), Observations of frequency-dependentSnpropagation in Northern Tibet, *Geophysical Journal International*, *179*(1), 475-488, doi:10.1111/j.1365-246X.2009.04318.x.

Bendick, R., and L. Flesch (2007), Reconciling lithospheric deformation and lower crustal flow beneath central Tibet, *Geology*, *35*(10), 895, doi:10.1130/g23714a.1.

Burg, J. P., and T. V. Gerya (2005), The role of viscous heating in Barrovian metamorphism of collisional orogens: thermomechanical models and application to the Lepontine Dome in the Central Alps, *Journal of Metamorphic Geology*, *23*(2), 75-95, doi:10.1111/j.1525-1314.2005.00563.x.

Chen, W.-P., M. Martin, T.-L. Tseng, R. L. Nowack, S.-H. Hung, and B.-S. Huang (2010), Shear-wave birefringence and current configuration of converging lithosphere under Tibet, *Earth and Planetary Science Letters*, *295*(1-2), 297-304, doi:10.1016/j.epsl.2010.04.017.

Chevrot, S., and L. Zhao (2007), Multiscale finite-frequency Rayleigh wave tomography of the Kaapvaal craton, *Geophysical Journal International*, *169*(1), 201-215, doi:10.1111/j.1365-246X.2006.03289.x.

Clark, M. K., J. W. M. Bush, and L. H. Royden (2005), Dynamic topography produced by lower crustal flow against rheological strength heterogeneities bordering the Tibetan Plateau, *Geophysical Journal International*, *162*(2), 575-590, doi:10.1111/j.1365-246X.2005.02580.x.

Clark, M. K., and L. H. Royden (2000), Topographic ooze: Building the eastern margin of Tibet by lower crustal flow, *Geology*, *28*(8), 703-706.

Forsyth, D. W., and A. Li (2005), Array Analysis of Two-Dimensional Variations in Surface Wave Phase Velocity and Azimuthal Anisotropy in the Presence of Multipathing Interference, in *Seismic Earth: Array Analysis of Broadband Seismograms*, edited by A. L. a. G. Nolet, AGU, Washington DC.

Gan, W., P. Zhang, Z.-K. Shen, Z. Niu, M. Wang, Y. Wan, D. Zhou, and J. Cheng (2007), Present-day crustal motion within the Tibetan Plateau inferred from GPS measurements, *Journal of Geophysical Research*, *112*(B8), doi:10.1029/2005jb004120.

Gerya, T. (2010), *Introduction to numerical geodynamic modelling*, xi, 345 p. pp., Cambridge University Press, Cambridge, UK ; New York.

Haines, S. S. (2003), INDEPTH III seismic data: From surface observations to deep crustal processes in Tibet, *Tectonics*, *22*(1), doi:10.1029/2001tc001305.

Huang, W.-C., et al. (2000), Seismic polarization anisotropy beneath the central Tibetan Plateau, *Journal of Geophysical Research*, *105*(B12), 27,979-927,989.

Hung, S.-H., F. A. Dahlen, and G. Nolet (2001), Wavefront healing: a banana-doughnut perspective, *Geophys. J. Int.*, *146*, 289-312.

Jimenez-munt, I., M. Fernandez, J. Verges, and J. Platt (2008), Lithosphere structure underneath the Tibetan Plateau inferred from elevation, gravity and geoid anomalies, *Earth and Planetary Science Letters*, *267*(1-2), 276-289, doi:10.1016/j.epsl.2007.11.045.

Kincaid, C., and P. Silver (1996), The role of viscous dissipation in the orogenic process, *Earth and Planetary Science Letters*, *142*, 271-288.

Kind, R., et al. (2002), Seismic images of crust and upper mantle beneath Tibet: evidence for Eurasian plate subduction, *Science*, *298*(5596), 1219-1221, doi:10.1126/science.1078115.

Kosarev, G., R. Kind, S. V. Sobolev, X. Yuan, W. Hanka, and S. Oreshin (1999), Seismic Evidence for a Detached Indian Lithospheric Mantle Beneath Tibet, *Science*, *283*(5406), 1306-1309, doi:10.1126/science.283.5406.1306.

Kumar, P., X. Yuan, R. Kind, and J. Ni (2006), Imaging the colliding Indian and Asian lithospheric plates beneath Tibet, *Journal of Geophysical Research*, *111*(B6), doi:10.1029/2005jb003930.

León Soto, G., E. Sandvol, J. F. Ni, L. Flesch, T. M. Hearn, F. Tilmann, J. Chen, and L. D. Brown (2012), Significant and vertically coherent seismic anisotropy beneath eastern Tibet, *J. Geophys. Res.*, *117*(B5), B05308, doi:10.1029/2011jb008919.

Li, A. (2011), Shear wave model of southern Africa from regional Rayleigh wave tomography with 2-D sensitivity kernels, *Geophysical Journal International*, *185*(2), 832-844, doi:10.1111/j.1365-246X.2011.04971.x.

Li, C., R. van der Hilst, A. Meltzer, and E. Engdahl (2008), Subduction of the Indian lithosphere beneath the Tibetan Plateau and Burma, *Earth and Planetary Science Letters*, *274*(1-2), 157-168, doi:10.1016/j.epsl.2008.07.016.

Liang, C., and X. Song (2006), A low velocity belt beneath northern and eastern Tibetan Plateau from Pn tomography, *Geophysical Research Letters*, *33*(22), doi:10.1029/2006gl027926.

Liang, X., E. Sandvol, Y. J. Chen, T. Hearn, J. Ni, S. Klemperer, Y. Shen, and F. Tilmann (2012), A complex Tibetan upper mantle: A fragmented Indian slab and no south-verging subduction of Eurasian lithosphere, *Earth and Planetary Science Letters*, *333-334*, 101-111, doi:10.1016/j.epsl.2012.03.036.

McNamara, D. E., W. R. Walter, T. J. Owens, and C. J. Ammon (1997), Upper mantle velocity structure beneath the Tibetan Plateau from Pn travel time tomography, *Journal of Geophysical Research*, *102*(B1), 493-505, doi:10.1029/96JB02112.

Molnar, P., and P. Tapponnier (1975), Cenozoic Tectonics of Asia: Effects of a Continental Collision, *Science*, *189*(4201), 419-429.

Montagner, J.-P., and L. Guillot (2002), Seismic Anisotropy and Global Geodynamics, *Reviews in Mineralogy and Geochemistry*, *51*, 353-385, doi:10.2138/gsrmg.51.1.353.

Nabelek, J., G. Hetenyi, J. Vergne, S. Sapkota, B. Kafle, M. Jiang, H. Su, J. Chen, and B.-S. Huang (2009), Underplating in the Himalaya-Tibet collision zone revealed by the Hi-CLIMB experiment, *Science*, *325*(5946), 1371-1374, doi:10.1126/science.1167719.

Nabelek, P. I., A. G. Whittington, and A. M. Hofmeister (2010), Strain heating as a mechanism for partial melting and ultrahigh temperature metamorphism in convergent orogens: Implications of temperature-dependent thermal diffusivity and rheology, *Journal of Geophysical Research*, *115*(B12), doi:10.1029/2010jb007727.

Nelson, K. D., et al. (1996), Partially molten middle crust beneath southern Tibet: Synthesis of Projest INDEPTH results, *Science*, *274*, 1684-1688.

Ni, J., and M. Barazangi (1984), Seismotectonics of the Himalayan collision zone: Geometry of the underthrusting Indian Plate beneath the Himalaya, *Geology*, *89*(B2), 1147-1163, doi:10.1029/JB089iB02p01147.

Nolet, G., and F. A. Dahlen (2000), Wave front healing and evolution seismic delay times *Journal of Geophysical Research*, *105*(B8), 19,043-019,054.

Priestley, K., E. Debayle, D. McKenzie, and S. Pilidou (2006), Upper mantle structure of eastern Asia from multimode surface waveform tomography, *Journal of Geophysical Research*, *111*(B10), doi:10.1029/2005jb004082.

Saito, M. (1988), *DISPER80: A subroutine package for the calculation of seismic normal-mode solutions*, Elsevier, New York.

Silver, P. G. (1996), Seismic anisotropy beneath the continents: Probing the depths of geology, *Annu. Rev. Earth Planet. Sci.*, *24*, 385-432, doi:10.1146/annurev.earth.24.1.385.

Sol, S., et al. (2007), Geodynamics of the southeastern Tibetan Plateau from seismic anisotropy and geodesy, *Geology*, *35*(6), 563, doi:10.1130/g23408a.1.

Styron, R., M. Taylor, and K. Okoronkwo (2010), Database of active structures from the Indo-Asian collision, *EOS Trans., AGU*, *91*(20), 181-182, doi:10.1029/2010EO200001.

Tapponnier, P., X. Zhiqin, F. Roger, B. Meyer, N. Arnaud, G. Wittlinger, and Y. Jingsui (2001), Oblique stepwise rise and growth of the Tibet plateau, *Science*, *294*(5547), 1671-1677, doi:10.1126/science.105978.

Tilmann, F., et al. (2003), Seismic Imaging of the Downwelling Indian Lithosphere Beneath Central Tibet, *Science*, *300*(5624), 1424-1427.

Turner, S., N. Arnaud, J. Liu, C. Hawkesworth, N. Harris, S. Kelly, P. V. Calsteren, and W. Deng (1996), Post-collision, Shoshonitic Volcanism on the Tibetan Plateau: Implications for Convective Thinning of the Lithosphere and the Source of Ocean Island Basalts, *Journal of Petrology*, *37*(1), 45-71.

Whittington, A. G., A. M. Hofmeister, and P. I. Nabelek (2009), Temperature-dependent thermal diffusivity of the Earth's crust and implications for magmatism, *Nature*, *458*(7236), 319-321, doi:10.1038/nature07818.

Wittlinger, G., et al. (1996), Seismic tomopraphy of northern Tibet and Kunlun:evidence for crustal blocks and matle velocity contrasts, *Earth and Planetary Science Letters*, *139*, 263-279.

Yang, Y. J., and D. W. Forsyth (2006), Regional tomographic inversion of the amplitude and phase of Rayleigh waves with 2-D sensitivity kernels, *Geophys. J. Int.*(166), 1148-1160.

Yang, Y., et al. (2010), Rayleigh wave phase velocity maps of Tibet and the surrounding regions from ambient seismic noise tomography, *Geochemistry Geophysics Geosystems*, *11*(8), doi:10.1029/2010gc003119.

Yin, A., and T. M. Harrison (2000), Geologic Evolution of the Himalayan-Tibetan Orogen, *Annu. Rev. Earth Planet. Sci., 28:211-280*.

Yue, H., et al. (2012), Lithospheric and upper mantle structure of the northeastern Tibetan Plateau, *J. Geophys. Res.*, *117*(B5), B05307, doi:10.1029/2011jb008545.

Zhao, J., et al. (2010), The boundary between the Indian and Asian tectonic plates below Tibet, *PNAS*, *107*(25), 11229-11233, doi:10.1073/pnas.1001921107/-/DCSupplemental.

Zhao, W., et al. (2011), Tibetan plate overriding the Asian plate in central and northern Tibet, *Nature Geosci*, *4*(12), 870-873, doi:10.1038/NGEO1309.

Zhou, H., and M. Murphy (2005), Tomographic evidence for wholesale underthrusting of India beneath the entire Tibetan plateau, *Journal of Asian Earth Sciences*, *25*(3), 445-457, doi:10.1016/j.jseaes.2004.04.007.

Zhu, L., and D. V. Helmberger (1998), Moho Offset Across the Northern Margin of the Tibetan Plateau, *Science*, *281*, 1170-1172.

2.8. Supplementary Figures
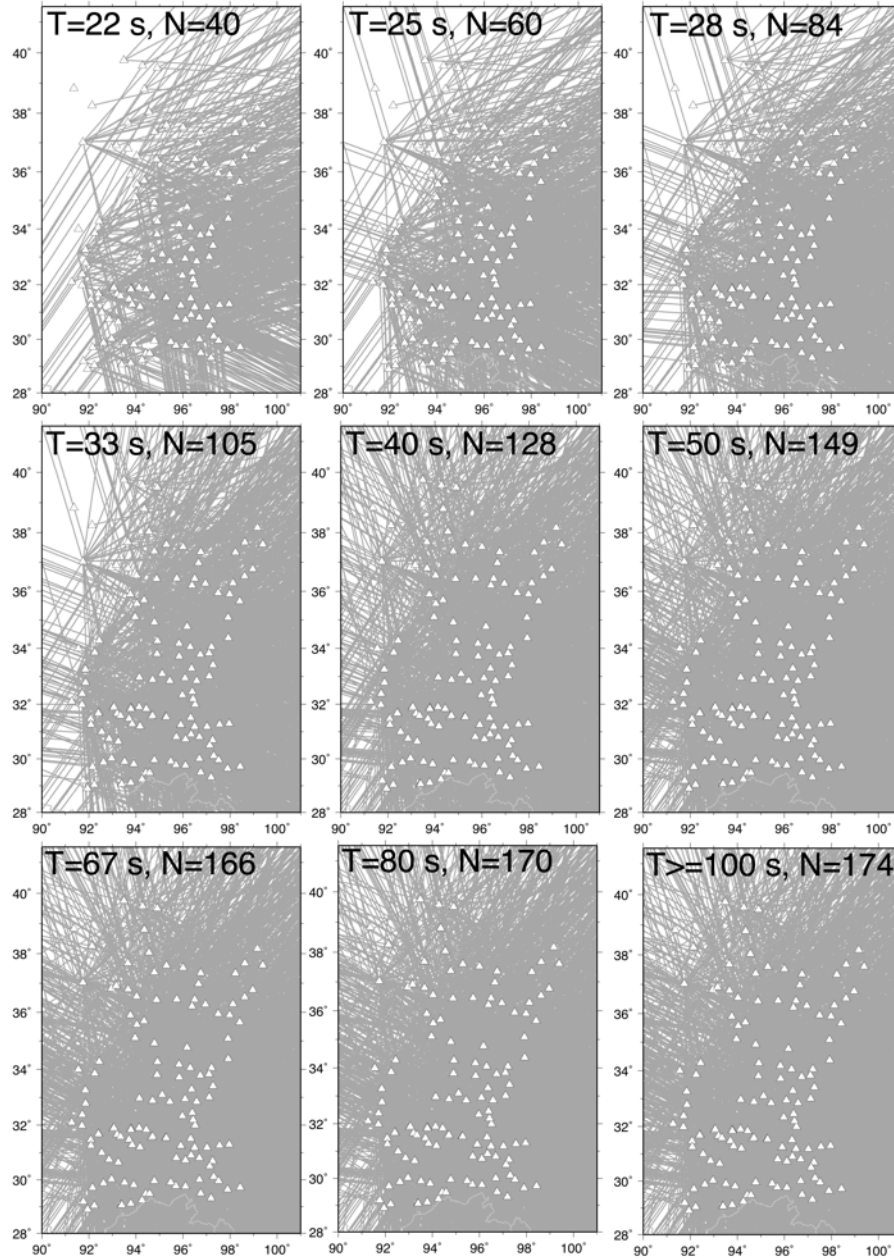
Supp. Figure 2.1. Ray path coverage for each period (T) with the number of events (N). Isotropic phase velocities are stable for T>=25 s (the periods with N>=60 earthquakes). White triangles show the seismic station locations. For periods less than 40 seconds, there is not enough coverage on northwestern edge of seismic array.
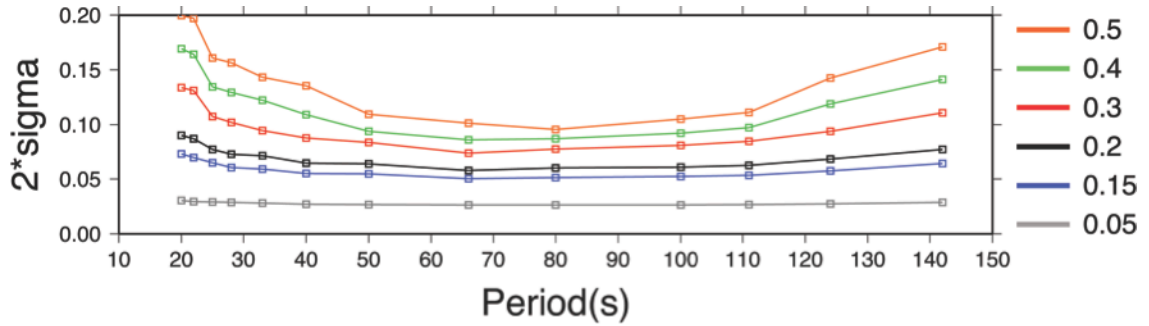
Supp. Figure 2.2. Model misfits (2σ) vs. period for different damping parameter values. Color codes are shown in the figure legend. Note that damping and damping parameter are inversely proportional (i.e. lower damping parameter values mean higher damping). As expected, model misfits decrease as damping increases (damping parameter decreases). Considering the consistency between ANT and TPWT results, and the model misfits, we determine that 0.2 is the most suitable damping parameter value. Moreover, all features discussed in the manuscript are consistently observed in all inversions.
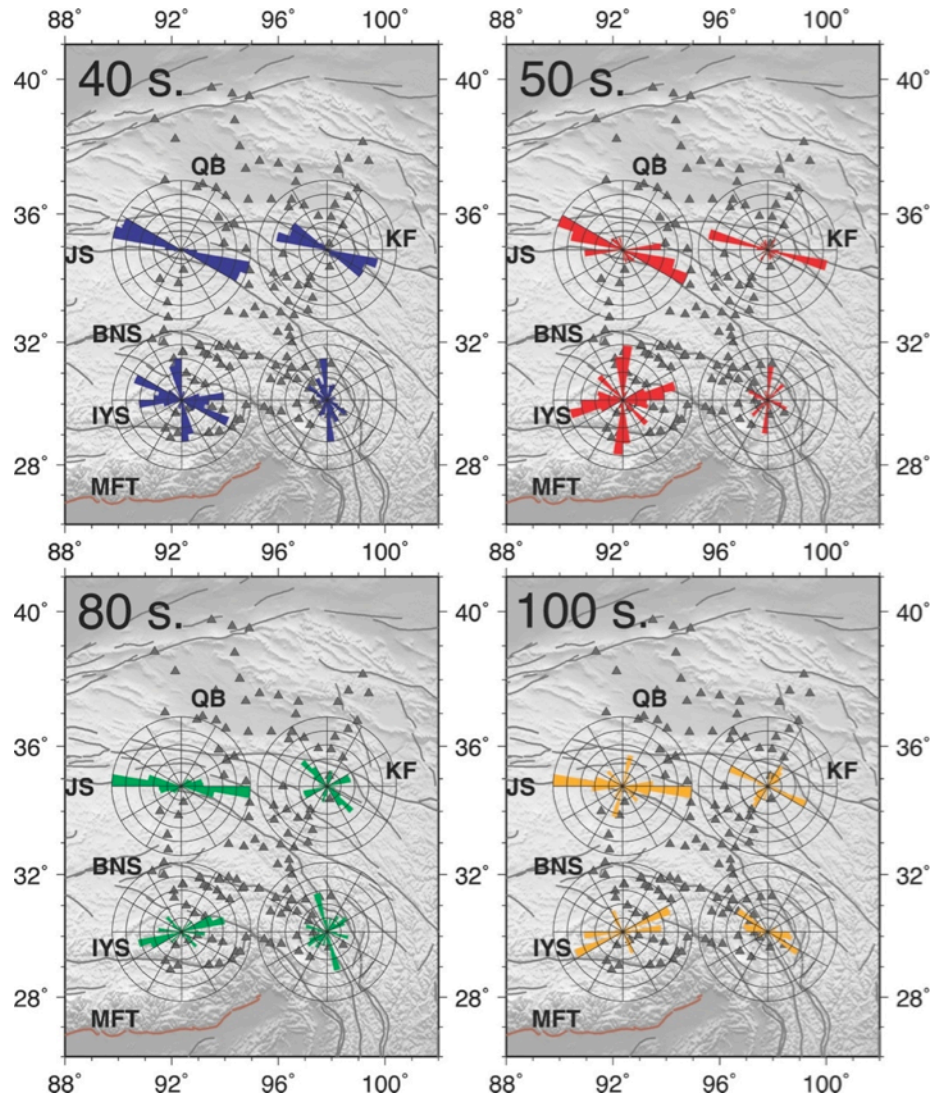
Supp. Figure 2.3. The distribution of azimuthal fast directions on sector diagrams for periods of 40 s, 50 s, 80 s, and 100 s. Note that sector diagrams are polar histograms; therefore, all values at each bin interval (in my case 10 degrees) were averaged prior to plotting. Moreover, in order to provide a better representation of relative anisotropy amplitudes, we normalized the sector plots for each period. The sector diagrams are centered in the sub-regions. Their diameters approximately indicate the sub-regions used.
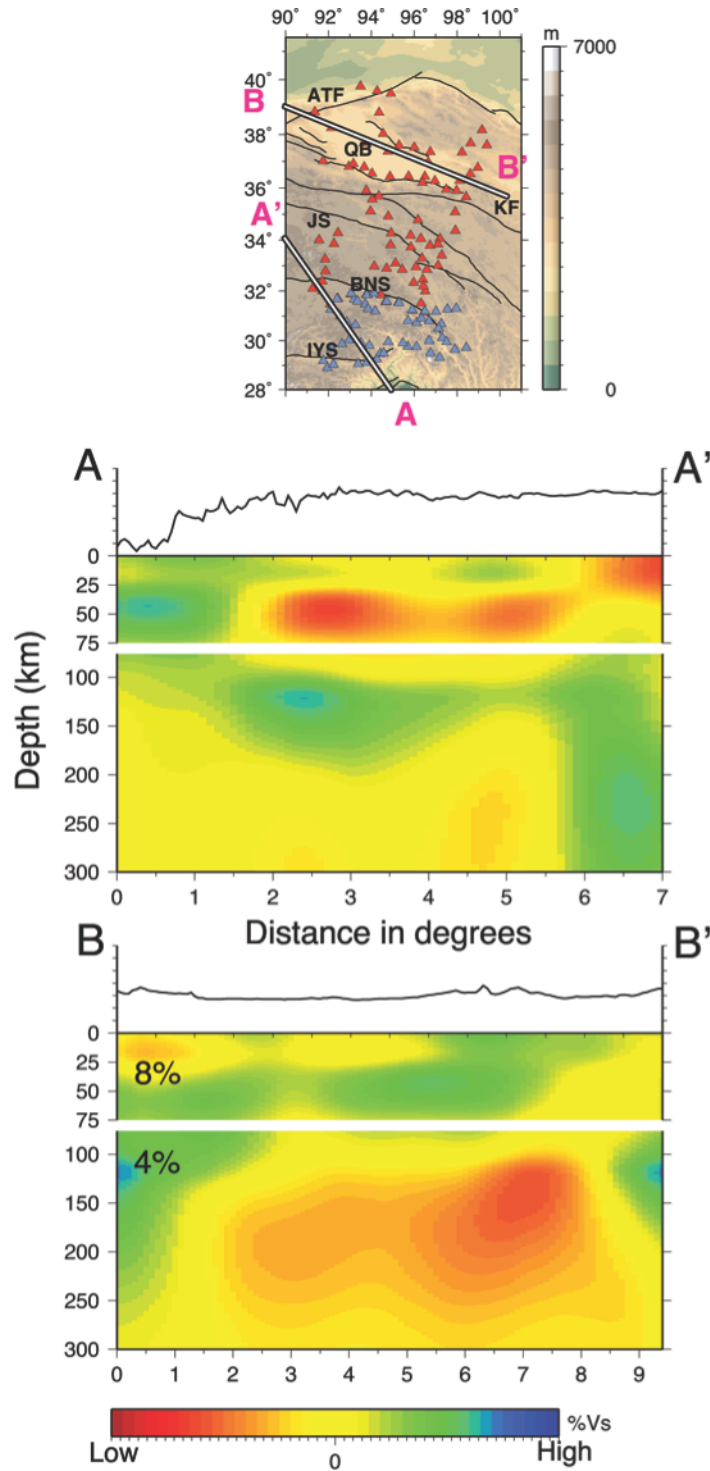
Supp. Figure 2.4. Two depth cross-sections across the high velocity body that represents the Indian plate (HVB1, A-A') and Qaidam Basin (B-B'). Top panel shows the locations of cross-sections. Horizontal axes in the cross-sections are the distance along the profile in degrees. Anomalies are drawn from surface to 75 km and 76-300 km using ±8% and ±4% variation, respectively.
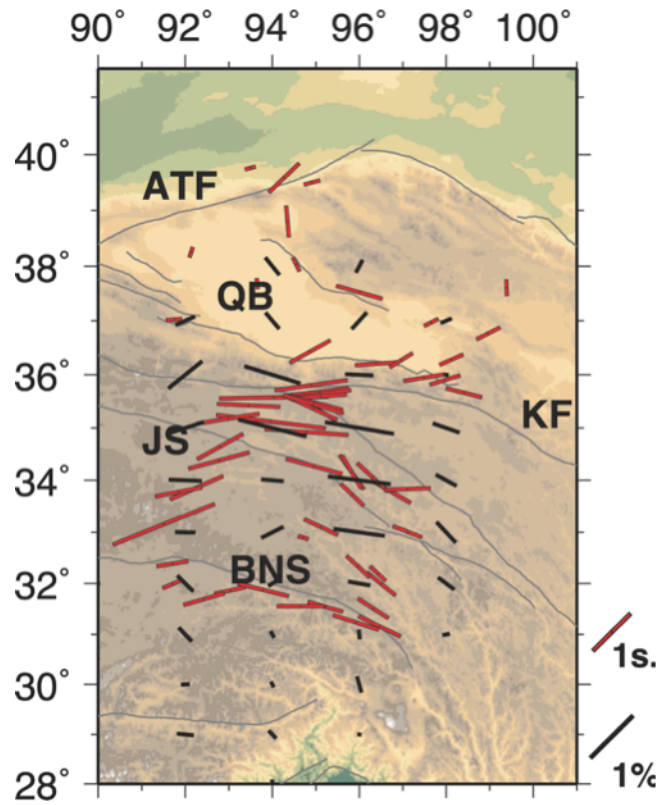
Supp. Figure 2.5. The comparison of azimuthal fast directions from this study (black bars, using the results from the period of 143 s) and shear wave splitting results of *Leon-Soto et al.*[2012] (red bars). The general clockwise rotation of seismic fast directions is consistent with shear-wave splitting results.
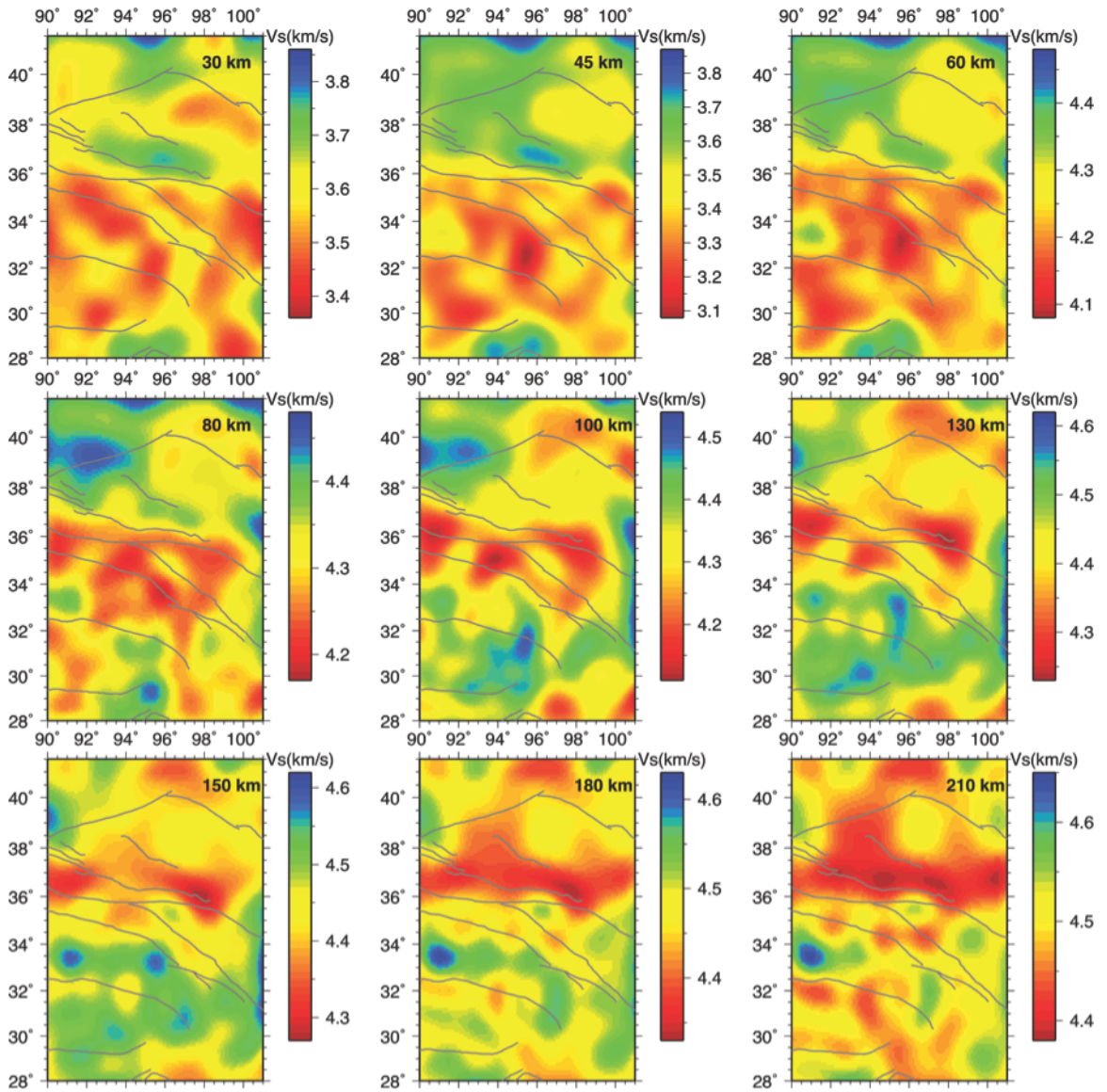
Supp. Figure 2.6. Unmasked map views of shear wave velocities presented in the paper for depths 30-210 km.

Chapter 3: 3D resolution tests of two-plane wave tomography using synthetic seismograms[2]

Abstract

Two-plane wave tomography (TPWT) has become a standard approach for obtaining fundamental mode Rayleigh wave phase velocities for regional studies. However, existing techniques for measuring TPWT's resolution do not demonstrate true capabilities of this method. Additionally, its applicability to Love waves has not been studied sufficiently.

Here, I calculate synthetic seismograms, resolving periods grater than ~30 s, to determine limitations of TPWT and its applicability to Love waves. I then calculate the surface wave dispersion employing TPWT and invert for shear wave speed. I use a modified version of the method for Love waves, decomposing the plane wave solutions into two perpendicular components. I show that, using Rayleigh waves, the method can successfully retrieve SV anomalies down to ~200 km. Below these depths, I observe both lateral and vertical smearing. Moreover, the method exhibits adequate resolution for SH waves down to ~100 km. These findings suggest that TPWT can be used for determining radial anisotropy in the uppermost mantle. Smearing is more evident in SH results than those of SV waves, probably due to longer wavelengths and shallower depth sensitivity of Love waves.

3.1. Introduction

Traditional surface wave tomography assumes that surface waves contain all frequencies and propagate along infinitely thin paths between source and receiver. This approach breaks down when the sizes of heterogeneities are comparable to or smaller than the dominant wavelength of surface waves [*Li*, 2011]. TPWT does not use the ray path approach, and so does not make these assumptions. Rather, it assumes that distortion of an incoming wave field can be expressed as the sum of two plane waves [*Forsyth*, 1998; *Forsyth and Li*, 2005], reducing the surface wave propagation problem to three unknowns for each plane wave: amplitude and phase differences with respect to a reference station, and deviation angle from the great circle path.

Since its introduction by *Forsyth* [1998], TPWT has been successfully applied in a variety of tectonic settings, including continental collision [*Ceylan et al.*, 2012] and subduction zones [*Calixto et al.*, 2013], cratons [*Li*, 2011], and mid-ocean ridges [*Forsyth* 1998; *Forsyth and Li*, 2005]. To account for finite frequency effects, earlier versions of TPWT employed Gaussian sensitivity kernels [*Forsyth*, 1998; *Forsyth and Li*, 2005]. Through derivation of single scattering (Born) kernels [*Zhou et al.*, 2004], latter versions of TPWT are able to account for scattering more effectively and hence yield improved images of the earth structure with improved model misfits [*Yang and Forsyth*, 2006].

Determining the true resolution of TPWT is critical to being able to correctly interpret the models generated by this method. Previous studies have estimated the resolution using either a pseudo-checkerboard test or model resolution matrix as measures of resolution. Pseudo-checkerboard tests measure lateral resolution for each frequency band by testing only the tomographic resolution as a function of ray coverage.

This approach does not provide any information about depth resolution. Similarly, model resolution matrices show relative variations in model parameter resolution assuming that forward modeling works perfectly, but do not contain information concerning the effective recoverable anomaly sizes. For these reasons, neither approach can reliably measure the true resolving power of the TPWT. Moreover, there have been only a few studies attempting to investigate TPWT's applicability to Love waves [*Li,* 2010; *Li and Li*, 2012], but none have performed an actual resolution test.
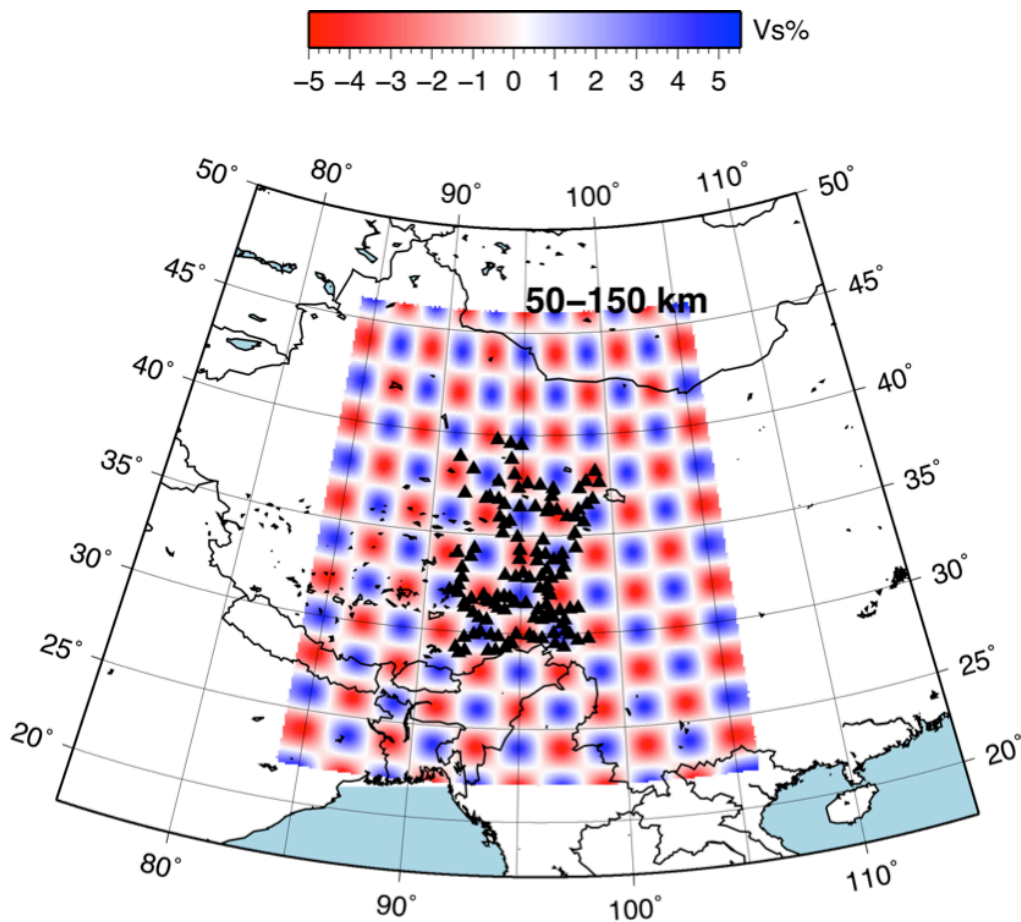

Figure 3.1. The hypothetical study area with underlying checkerboard structure between 50-150 km. Black triangles show the seismic stations from Namche Barwa [*Sol et al.*, 2007] and INDEPTH-IV arrays. For an example of meshes used in calculations, see Supp. Fig. 3.1.

In this study, I investigate abilities of TPWT using synthetic seismograms for an isotropic checkerboard earth model. I employ TPWT for measuring Love and Rayleigh wave dispersion, and calculating SH and SV wave speeds. Using this approach, I address the following questions: (1) how reliable is TPWT and what is the minimum anomaly size that can be recovered with such reliability, (2) how many events are required for obtaining robust results, and (3) what are the limitations of TPWT when applied to Love waves?
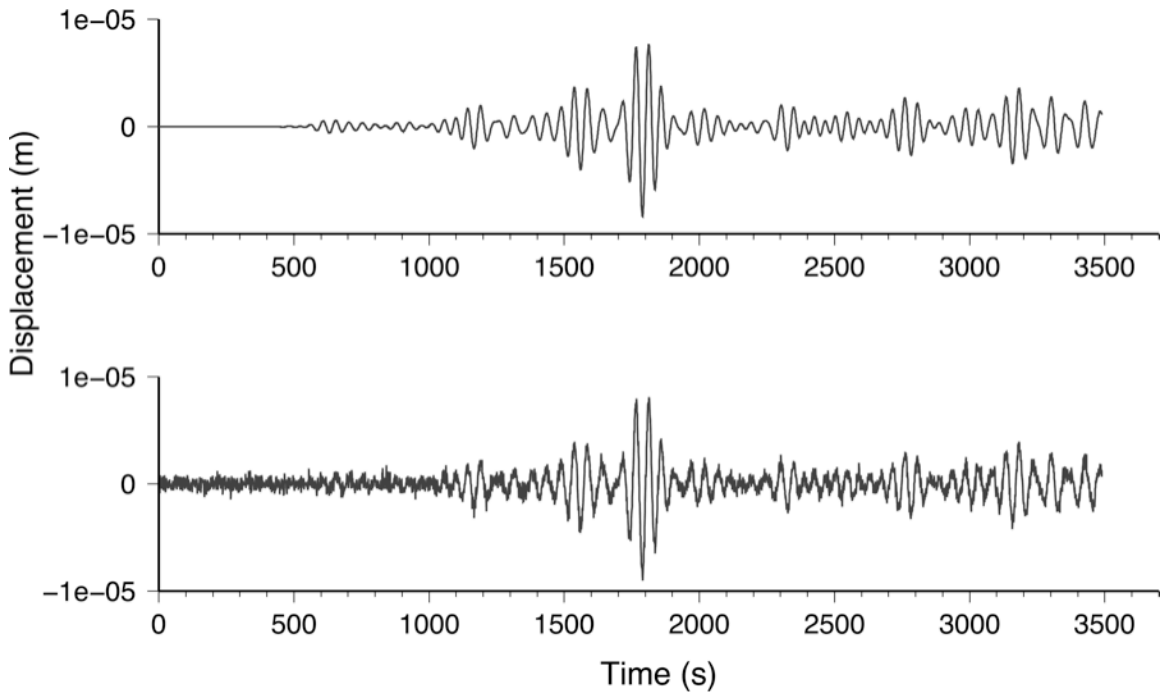

Figure 3.2. An example of synthetic seismogram before (top panel) and after (bottom panel) adding noise. The S/N ratio in the bottom seismogram is 15.

50

3.2. Synthetic data and methods

I calculate synthetic seismograms with SPECFEM3D software [*Tromp et al.*, 2008] for the same event-receiver pairs incorporated in *Ceylan et al.* [2012]'s work. They combine records from INDEPTH-IV and Namche Barwa [*Sol et al.*, 2007] arrays for applying TPWT to E. Tibetan Plateau (Figure 3.1). Specifically, they use events with epicentral distances between 20° and 120°, depths $\leq$ 100 km, and $M_S \geq 5.7$. In order to build synthetic data sets, I construct isotropic earth models with a checkerboard upper mantle extending from 50 to 550 km. These checkerboards have cell sizes that vary between 1°x1° and 3°x3° laterally, and 50-150 km vertically. Further, I take PREM [*Dziewonski and Anderson*, 1981] as the background model, and use a velocity perturbation of ±5% (Supp. Fig. 3.1). To add more structural complexity, hypothetical earth models are about two times larger than the region in interest (~22°x22°; Figure 3.1). I use a flat Moho located at 50 km for all of my synthetic models. With these parameters, the shortest period I can reliably resolve is ~30 s.

Following the generation of synthetic seismograms, I add Gaussian noise to each recording by assigning a randomly selected S/N ratio (> 15, Figure 3.2). I then employ a semi-automatic windowing algorithm (see Appendix 3.A1) to process transverse and vertical components of synthetic data across 16 frequency bands for periods between 33 s and 167 s. This windowing algorithm greatly reduces the time for processing TPWT data. Because filter widths may introduce artificial errors into dispersion measurements, I employ 3-mHz- and 10-mHz-wide Butterworth filters for periods > 67 s and $\leq$ 67 s, respectively (see Appendix 3.A2).

The first step in my inversions is calculating 1D average dispersion curve with Gaussian sensitivity kernels. I then use these results to calculate Born sensitivity kernels for Rayleigh and Love waves [*Zhou et al.*, 2004] (Figure 1.2). In the case of Rayleigh waves, the polarization terms in sensitivity kernels for initial and scattered waves can be neglected, as they are equal [*Yang and Forsyth*, 2006]. For Love waves, on the other hand, the polarization term for scattered waves is a function of their scattering angles [*Snieder*, 1986]. I incorporate these kernels in the next step of my inversions to account for finite frequency effects.

The second step of the tomographic inversions involves determining 2D isotropic phase wave speeds for each frequency (Supp. Fig. 3.2). In reality, horizontal components contain more noise than the vertical; hence number of events used for Love waves may be less than Rayleigh waves. Therefore, I included 170 and 120 events for Rayleigh and Love wave phase velocity inversions, respectively. I use a constant smoothing length of 80 km for both sensitivity kernels and phase wave speeds. I calculate the amplitude and phase variations with respect to a reference station to avoid dependence on the source magnitude. I choose the reference station for each event based on the minimum RMS misfit in amplitudes with respect to the mean value. Then, I construct a local Cartesian coordinate system, where the reference station is the origin, x direction is along the great circle path between event and the reference station, and y direction is 90° counterclockwise from x.
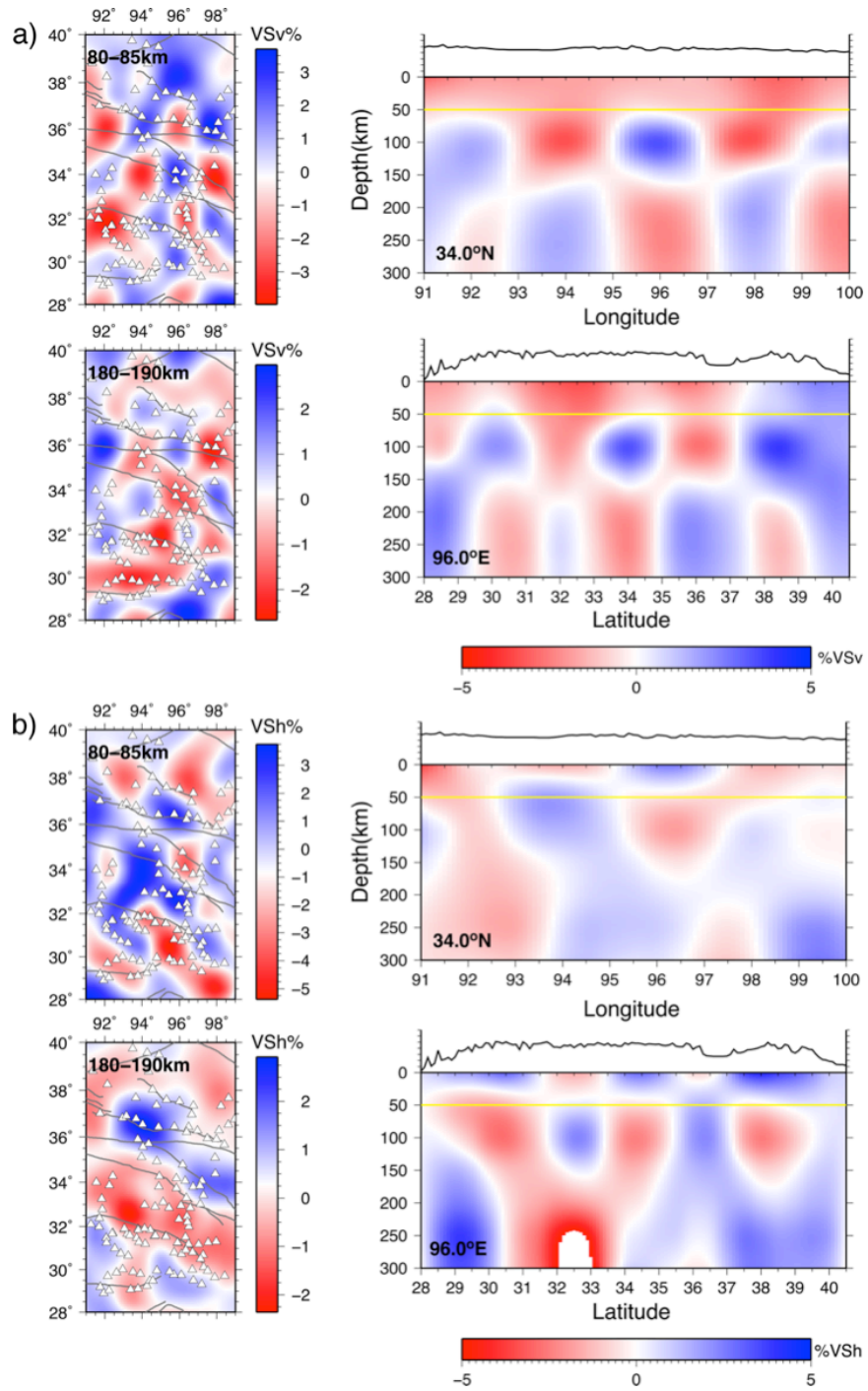
Figure 3.3. Resolution test results for a) Rayleigh waves, and b) Love waves. The heterogeneities in the input model are 2°x2°x100 km, with a velocity variation of 5%. The cross-sections are along 34°N and 96°E, respectively. Depths of cross-sections are indicated on top left corners of each panel. More images are provided in Supp. Fig. 3.4. The solid yellow line in cross-sections indicates the Moho depth (50 km).

For Rayleigh waves, particle motions fall on the same plane as plane waves. However, Love waves are on a transverse plane and their particle motion vector is perpendicular to the propagation direction and the wave field. Therefore, the assumption of sum of two-plane waves cannot be applied directly. To overcome this limitation, I rotate the windowed transverse components to x and y directions of local coordinate system [*Li,* 2010], inverting for both plane wave solutions. I calculate the final phase wave speeds by averaging these two components.

The third and last step of the inversion is obtaining shear wave velocities using isotropic phase maps from the second step (Figure 3.3). For shear wave inversion, I use partial derivatives from *Saito*[1988] (DISPER80 algorithm). One necessary step in inverting phase and group velocities for shear wave speeds is to adapt AK135 to be used as initial earth model for the linearized least squares inversion. Hence, although the background model in my simulations is PREM, I follow the same procedure assuming I have the knowledge of Moho depth (50 km in the synthetic models).

3.3 Test results

Essentially, TPWT in conjunction with Rayleigh waves can sufficiently recover anomalies for regional tomography purposes. Love waves, however, require a modified version of TPWT, and both lateral and vertical resolution has poorer quality than Rayleigh waves (Figure 3.3).

My tests using Rayleigh waves show that the combination of TPWT and DISPER80 has good resolution down to ~200 km, for heterogeneities around or larger than ~2° by 2° laterally, and 100 km vertically (Figure 3.3a). Below ~200 km, I observe

evidence of vertical smearing (for additional images see Supp. Fig. 3.4-3.6). Furthermore, I could not retrieve the checkerboard pattern for smaller anomalies (Supp. Fig. 3.3). Love waves exhibit poorer resolution than Rayleigh waves. The better-retrieved anomalies are rather confined to the center of seismic array. Vertically, SH resolution is adequate for imaging heterogeneities down to ~100-110 km (Figure 3.3b).

Direct application of TPWT to Love waves results in poor phase wave speed determination for longer periods (~ >50 s), consequently decreasing SH wave resolution. Long period noise on the transverse component, generally present in real cases, may limit retrieval of any detail in phase wave speed (Supp. Fig 3.7). My findings confirm that *Li* [2010]'s method of decomposing two plane wave solutions into two components provides more robust results. However, I observe a lateral shift of ~1° in the location of anomalies. Additionally, Love wave anomalies are more strongly affected by deeper structures than Rayleigh waves.

Residuals of phase maps are inversely proportional to the number of events. According to my observations, TPWT gives robust results at a threshold of ~50 earthquakes. For Rayleigh waves, the average 2σ errors for 100 s (where σ is the standard deviation) were reduced from 0.18 to 0.07 km/s using 15 and 50 events, respectively.

These results allow us to compare traditional surface wave tomography with TPWT, and further explore the potential use of the method in radial anisotropy studies.

55

3.4. Discussion

My resolution tests using full waveform simulations strongly suggest that TPWT can resolve anomalies at an order of 2°x2°x100 km, to depths of at least 200 km for Rayleigh waves (Figure 3.3a). At these depths, the shortest dominant period is ~143 s with wavelengths > 400 km (taking an average phase velocity of 4.0 km/s). My results show TPWT can recover anomalies smaller than the dominant wavelength, where traditional approaches break down. Contrary to some approaches, TPWT employs both amplitude and phase information, rather than the ray path theory. Depending on whether or not the plane waves are in phase, wave fields may interfere both constructively and destructively with one another, creating a gradually variable spatial pattern [*Forsyth and Li*, 2005]. Such patterns can be expressed as the sum of planar waves within minor deviations from great circle paths. Furthermore, spatial overlapping of such interferences enhances resolution. For these reasons, I suggest TPWT is more efficient than traditional approaches for regional studies.

If seismic noise on transverse components dominates the signal, TPWT cannot detect variations in phase wave speed when directly applied. *Li* [2010] suggests Love waves should be treated in two different components, rotated to x and y directions of the local coordinate system. I have tested both direct application and two-component approach in my simulations. Using noise-free synthetic seismograms, I do not detect a major difference between these two treatments of TPWT. However, as I increase long period noise, direct application of TPWT results start to degrade, recovering little to no information about earth structure. Hence, my findings support *Li* [2010], by indicating that long period noise has more effects on Love than Rayleigh waves. This effect is

further compounded by the existence of long period tilt on many horizontal component seismograms. Tilt occurs at frequencies less than ~0.02 Hz, thus making signal to noise in the longer periods typically lower for horizontal component as compared to vertical component seismograms. Given these limitations, I suggest that TPWT can potentially be applied for calculating radial anisotropy in the uppermost mantle (for anomalies > 2°). However, further tests are required for radially anisotropic earth models. In my ideally isotropic synthetic models, I observed artificial radial anisotropy (SH > SV) due to variations in the damping parameter. The choice of damping parameter might be very problem specific and I find it difficult to provide rigid constraints using my synthetic tests.

Crustal structures retrieved using Love waves are highly affected by the underlying mantle (Figure 3.3.b). Although the checkerboards are located solely in the mantle (50-550 km) in my synthetic models, I observe apparent effects of deeper structure at crustal depths. On the other hand, when combined with Rayleigh waves, TPWT successfully recovers the earth model around Moho (Figure 3.3.a) with lesser effects from the underlying mantle. I suggest that this apparent structure is due to shallower depth sensitivity of Love waves compared to Rayleigh waves.

An additional difficulty of TPWT is determining actual resolution of the method. Traditional checkerboard tests include calculating phase and amplitude of real data, then replacing initial model for inversion with a checkerboard structure. Outcomes indicate phase velocity resolution of each frequency. In other words, this approach assumes that the earth structure consists of checkerboards as thick as dominant depth sensitivity of target frequencies. Therefore, using synthetic seismograms for resolution purposes is a

57

more realistic method for measuring TPWT's resolution. Additionally, my findings are valuable for arrays with similar inter-station spacing and study area size.

Here, I discuss that TPWT gives robust results when ~50 or more events are used. For regional tomography purposes, it requires less data than traditional approaches. I suggest that TPWT can successfully recover anomalies down to ~200 km for Rayleigh waves. On the other hand, a modified version of TPWT provides more improved results using Love waves.

3.5. Conclusions

In this study, I tested TPWT using synthetic seismograms for both Rayleigh and Love waves. My conclusions are as follows:

(1) In conjunction with DISPER80, TPWT can reliably recover anomalies ~2°x2°x100 km, down to ~200 km depth using Rayleigh waves. Below these depths, I observe vertical smearing.

(2) The method can also be applied to Love waves, by decomposing two plane wave solution into two components along x and y directions. SH waves exhibit adequate resolution down to ~100 km.

(3) TPWT can potentially be applied to measure radial anisotropy for anomalies > 2° in the uppermost mantle.

(4) TPWT yields robust measurements when ~50 events or more are used.

3.6. Acknowledgements

3.7. References

Calixto, F. J., E. Sandvol, S. Kay, P. Mulcahy, B. Heit, X. Yuan, B. Coira, D. Comte, and P. Alvarado (2013), Velocity structure beneath the southern Puna plateau: Evidence for delamination, *Geochemistry, Geophysics, Geosystems*, n/a-n/a, doi:10.1002/ggge.20266.

Ceylan, S., J. Ni, J. Y. Chen, Q. Zhang, F. Tilmann, and E. Sandvol (2012), Fragmented Indian plate and vertically coherent deformation beneath eastern Tibet, *Journal of Geophysical Research*, *117*(B11), doi:10.1029/2012jb009210.

Dziewonski, A. M., and D. L. Anderson (1981), Preliminary reference Earth model, *Physics of The Earth and Planetary Interiors*, *25*(4), 297-356, doi:http://dx.doi.org/10.1016/0031-9201(81)90046-7.

Forsyth, D. W. (1998), Phase Velocities of Rayleigh Waves in the MELT Experiment on the East Pacific Rise, *Science*, *280*(5367), 1235-1238, doi:10.1126/science.280.5367.1235.

Forsyth, D. W., and A. Li (2005), Array Analysis of Two-Dimensional Variations in Surface Wave Phase Velocity and Azimuthal Anisotropy in the Presence of Multipathing Interference, in *Seismic Earth: Array Analysis of Broadband Seismograms*, edited by A. L. a. G. Nolet, AGU, Washington DC.

Komatitsch, D., G. Erlebacher, D. Goddeke, and D. Michea (2010), High-order finite-element seismic wave propagation modeling with MPI on a large GPU cluster, *Journal of Computational Physics*, *229*(20), 7692-7714, doi:http://dx.doi.org/10.1016/j.jcp.2010.06.024.

Li, A. (2010), Radial Anisotropy from Regional Surface Wave Tomography with the Presence of Multipathing Interference, in *AGU Fall Meeting*, edited, San Francisco.

Li, A. (2011), Shear wave model of southern Africa from regional Rayleigh wave tomography with 2-D sensitivity kernels, *Geophysical Journal International*, *185*(2), 832-844, doi:10.1111/j.1365-246X.2011.04971.x.

Li, L., and A. Li (2012), Radial anisotropy in the northeastern Tibetan Plateau from surface wave tomography, in *AGU Fall Meeting*, edited, San Francisco.

Maggi, A., C. Tape, M. Chen, D. Chao, and J. Tromp (2009), An automated time-window selection algorithm for seismic tomography, *Geophysical Journal International*, *178*(1), 257-281, doi:10.1111/j.1365-246X.2009.04099.x.

Saito, M. (1988), *DISPER80: A subroutine package for the calculation of seismic normal-mode solutions*, Elsevier, New York.

Snieder, R. (1986), 3D Linearized scattering of surface waves and a formalism for surface wave holography, *Geophys. J. R. astron. Soc.*, *84*, 581-605.

Sol, S., et al. (2007), Geodynamics of the southeastern Tibetan Plateau from seismic anisotropy and geodesy, *Geology*, *35*(6), 563, doi:10.1130/g23408a.1.

Tromp, J., D. Komatitsch, and Q. Liu (2008), Spectral-Element and Adjoint Methods in Seismology, *Communications in Computational Physics*, *3*(1), 1-32.

Yang, Y., and D. W. Forsyth (2006), Regional tomographic inversion of the amplitude and phase of Rayleigh waves with 2-D sensitivity kernels, *Geophys. J. Int.*(166), 1148-1160.

Zhou, Y., F. A. Dahlen, and G. Nolet (2004), Three-dimensional sensitivity kernels for surface wave observables, *Geophysical Journal International*, *158*(1), 142-168, doi:10.1111/j.1365-246X.2004.02324.x.

3.8. Appendix 3.A1: Automatic windowing algorithm

In practice, surface wave arrivals are decided upon visual inspection of seismograms for a particular set of frequencies. This process is not very time efficient when dealing with large data sets. Therefore, using a pattern recognition technique similar to the one employed in FLEXWIN software [*Maggi et al.*, 2009], I developed a semi-automatic windowing algorithm (Figure 3.A1).
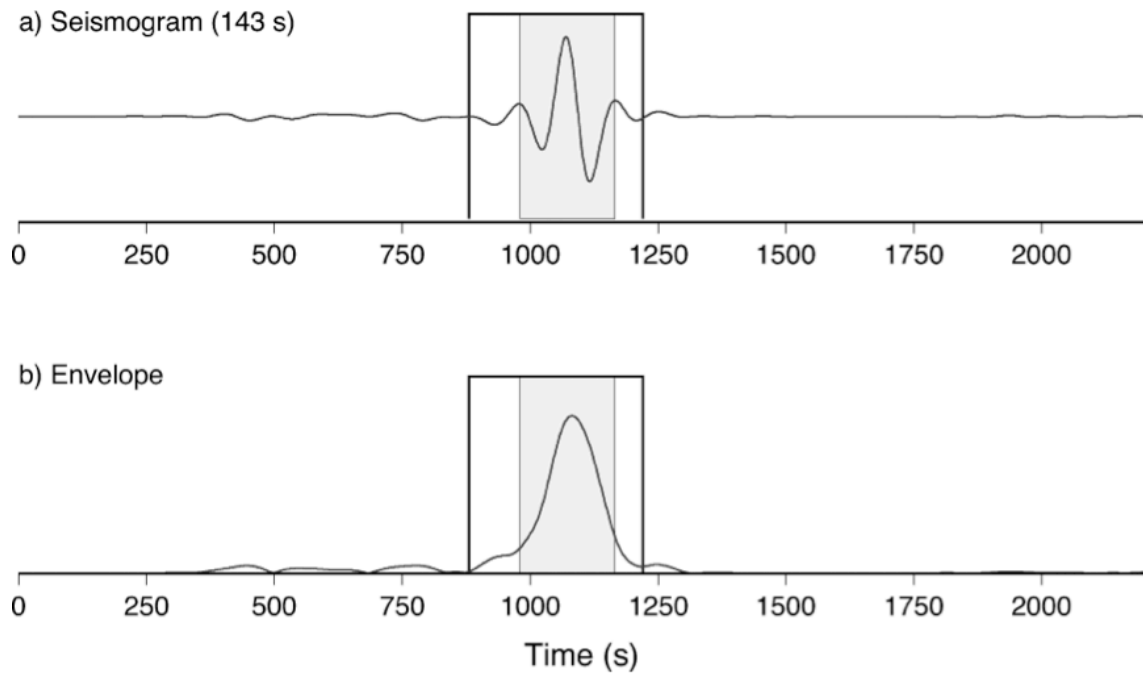

Figure 3.A1. A schematic of semi-automatic windowing algorithm. The top panel shows a vertical component seismogram, bandpass-filtered using a 10 mHz Butterworth filter centered at 0.007 Hz. The energy envelope of seismogram is shown in the bottom panel. Solid black rectangles and shaded gray boxes indicate initial and final choice of surface wave window, respectively.

The steps of my windowing algorithm are as follows:

1) Apply band-pass filter to seismograms for a target frequency.

2) Calculate the energy envelopes using Hilbert transform.

3) Detect minima and maxima of the energy envelope, and find the maximum amplitude. The geometry of energy envelope roughly indicates the arrival of surface waves (Figure 3.A1).

4) In order to detect surface arrival more accurately, find the minima on both sides of the maximum amplitude. Then, calculate the line equations between the maximum point and the two minima (Figure 3.A2).

5) Calculate the perpendicular distances between these lines and each point between the minima and the maximum (Figure 3.A2).

6) Detect the closest minima or maxima on the band-pass-filtered seismogram, corresponding to the points found in the previous step. For consistency, modify the arrival times and adjust window widths choosing peaks or troughs only.
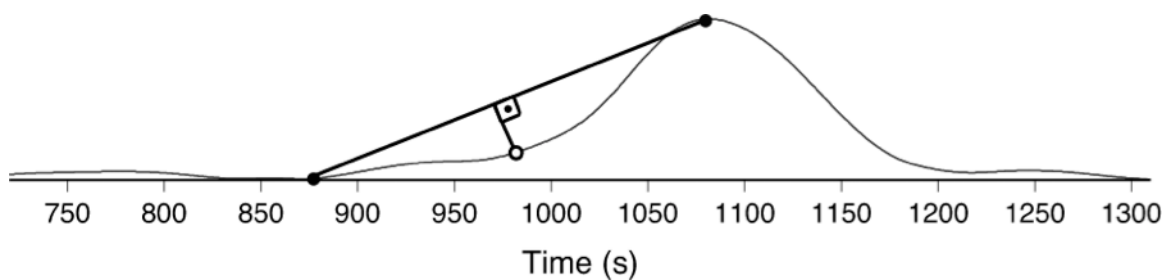

Figure 3.A2. A close-up look of the energy envelope shown in Figure 3.A1.b. Final choice of window start and end times are made using the points with the maximum perpendicular distances (open circle) to the lines between two minima and the maximum of energy envelope (closed circles). For simplicity, we plot only the left side of the envelope.

62

This algorithm assumes that surface wave arrivals are correlated with the maximum amplitude of energy envelopes. However, depending on the signal-to-noise ratios of individual seismograms, this assumption may not always hold; i.e. long period noise may cause larger amplitudes than the surface waves on the energy envelope. Therefore, although my method can be used to window seismograms full automatically, visual inspection is still crucial for accuracy.
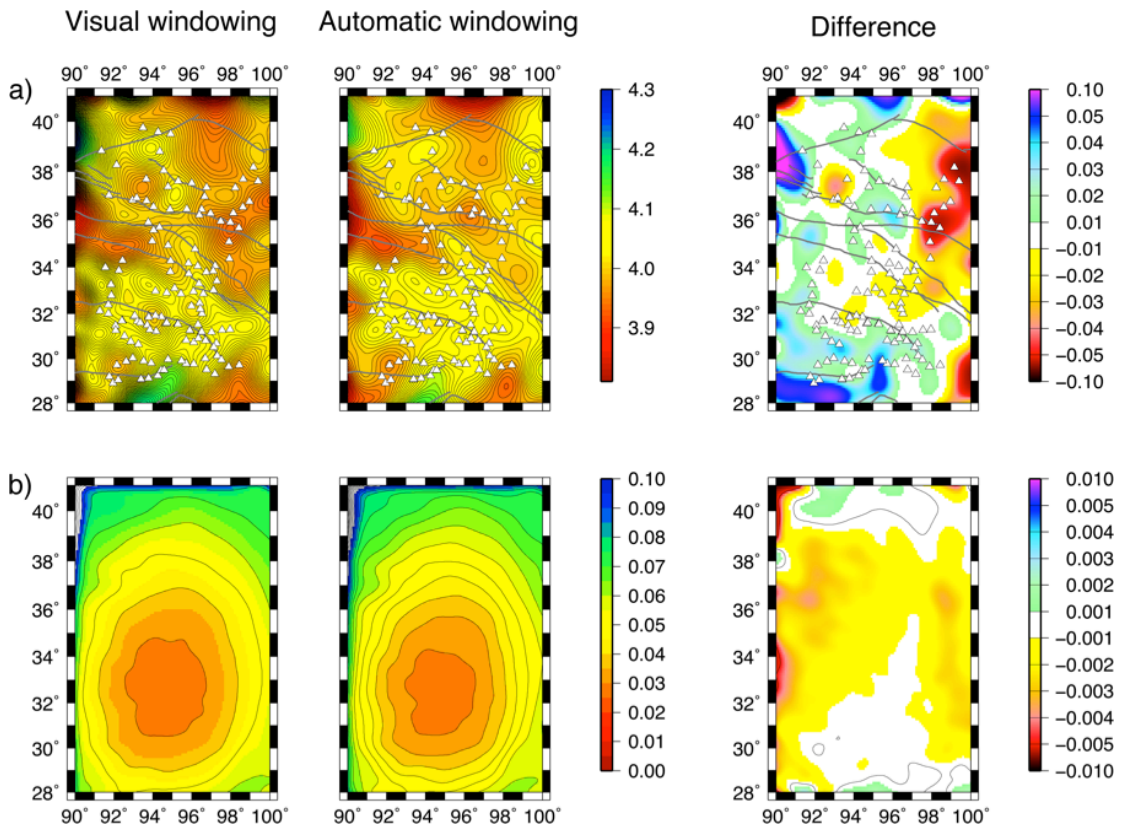

Figure 3.A3. A comparison of full automatic and visual windowing processes for isotropic Rayleigh phase wave speeds (T=100 s), using real data from INDEPTH-IV and Namche Barwa arrays. The first two columns are results from visually and full-automatically windowed data, respectively. Third column shows the difference between these two for a) phase maps, and b) 2σ errors, where σ is the standard deviation. All units are in km/s. We used 80 events for calculations.

To test the reliability of my algorithm, I visually selected 80 real events with high S/N ratios, from INDEPTH-IV and Namche Barwa arrays. I processed these earthquakes both visually and full-automatically. Figure A3.3 shows differences between these two methods in terms of phase wave speeds and errors, for T=100 s. Differences in phase wave speeds range between ± 0.045 km/s within the seismic array. Further, 2σ errors indicate that visual processing of data causes slightly less error than fully automatic windowing (~0.003 km/s). Given high S/N ratios, the fully automatic windowing process works for surface waves.

Surface wave arrivals with the most energy cause a slope change on envelope plots. These points where envelopes change their curvature are not minima or maxima, and they mark the surface wave window well. To detect these points, I calculate the maximum perpendicular distance of each point between the maximum and two minima of energy envelope (Figure 3.A2) in step 4. The practicality of this approach lies in its ability to detect the approximate locations where slope changes. An alternative method includes tracking slope along the envelope plot. However, it is hard to determine a slope threshold due to the variable geometry of envelopes. Moreover, this algorithm is conservative in terms of window widths, i.e. proposed windows may be too narrow. For my purposes, in step 6, I prefer enlarging window widths by widening from the center of windows.

3.9. Appendix 3.A2: Wide vs. narrow band-pass filters

In general, the studies employing TPWT use a 10 mHz-wide band-pass filter centered on some target frequency (e.g. *Ceylan et al.*, 2012; *Forsyth and Li*, 2005). However, if the filter is not sufficiently narrow, the dominant period within the frequency band becomes shorter (Figure 3.A4). Consequently, wide filtering introduces increased amplitudes and phase delays into the data set.
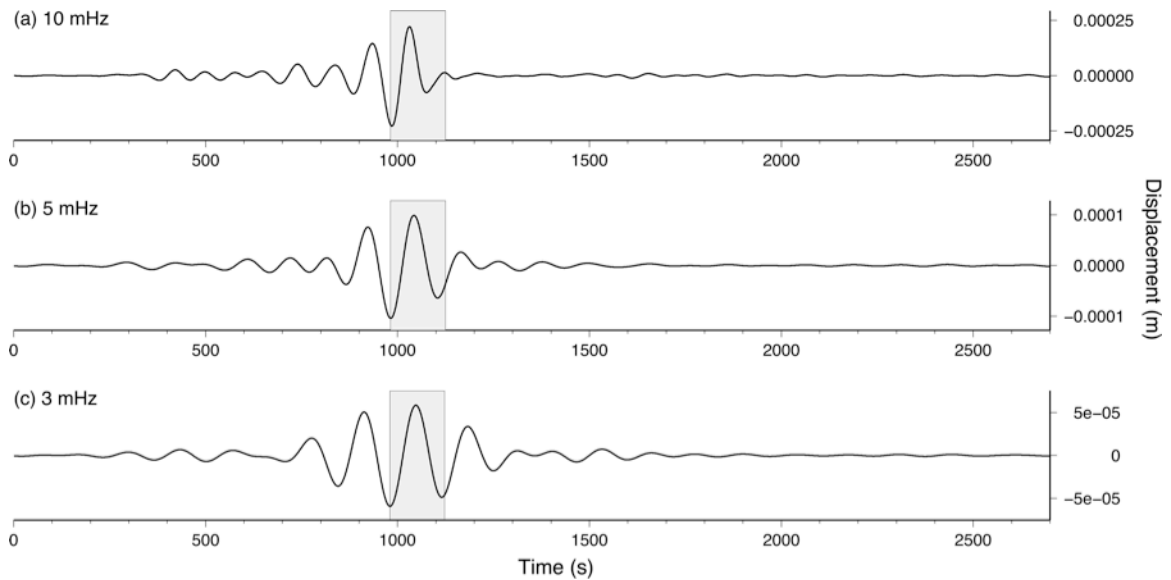

Figure 3.A4. Comparison of band-pass filtered data using different filter widths. All three panels above use a Butterworth filter centered at the period of 143 s. The gray boxes show one complete cycle at this period. The dominant period becomes shorter as window width increases.

I show effects of filter widths in Figure 3.A5. In the figure, I choose two stations from INDEPTH-IV array (C001 and F005). The stations are on the same great circle path (+- 15 degrees) with the event, resulting from strike slip faulting in Bismark Sea, Papua

New Guniea (Mw = 6.2 and epicentral distance of ~7000 km to the closest station, C001).

The distance between stations is ~300 km. I observe a ~5 s time delay difference

between narrow and wide filters, implying calculated wave speed would be ~10% slower

than the actual average phase wave speed. Hence, in particular, the seismic wave speeds

measured using the ray path approach may not represent wave speeds at targeted

frequencies.
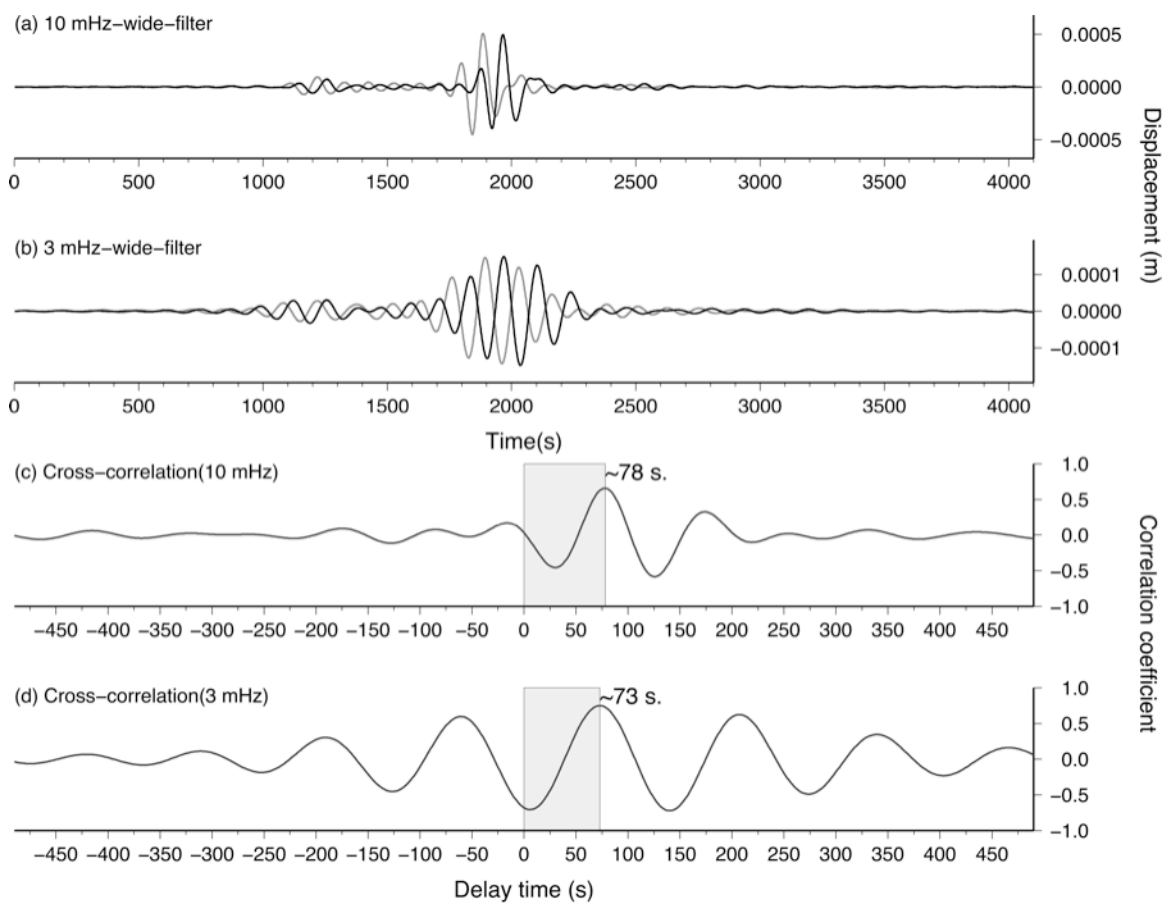
Figure 3.A5. Comparison of filtering effect for the period of 143 s using two stations on the same great circle path with the event (Mw=6.2, Bismark Sea). a) Filtered using a10-mHz-wide Butterworth filter, b) 3-mHz wide Butterworth applied, c) and d) Cross-correlations of seismograms in top two panels, respectively. 10 mHz-wide filter reveals a phase delay of ~ 5 s.

Experiments with real data [*Calixto et al.*, 2013] using different filter widths showed artificial flattening of dispersion curves due to filter widths. However, I found no significant difference using noise-free synthetic seismograms, suggesting that S/N ratio has an important role on filtering effects. Therefore, to increase accuracy of my surface wave dispersion measurements, I utilize a 3mHz-wide Butterworth filter for periods longer than 67 s.

3.10. Supplementary Figures
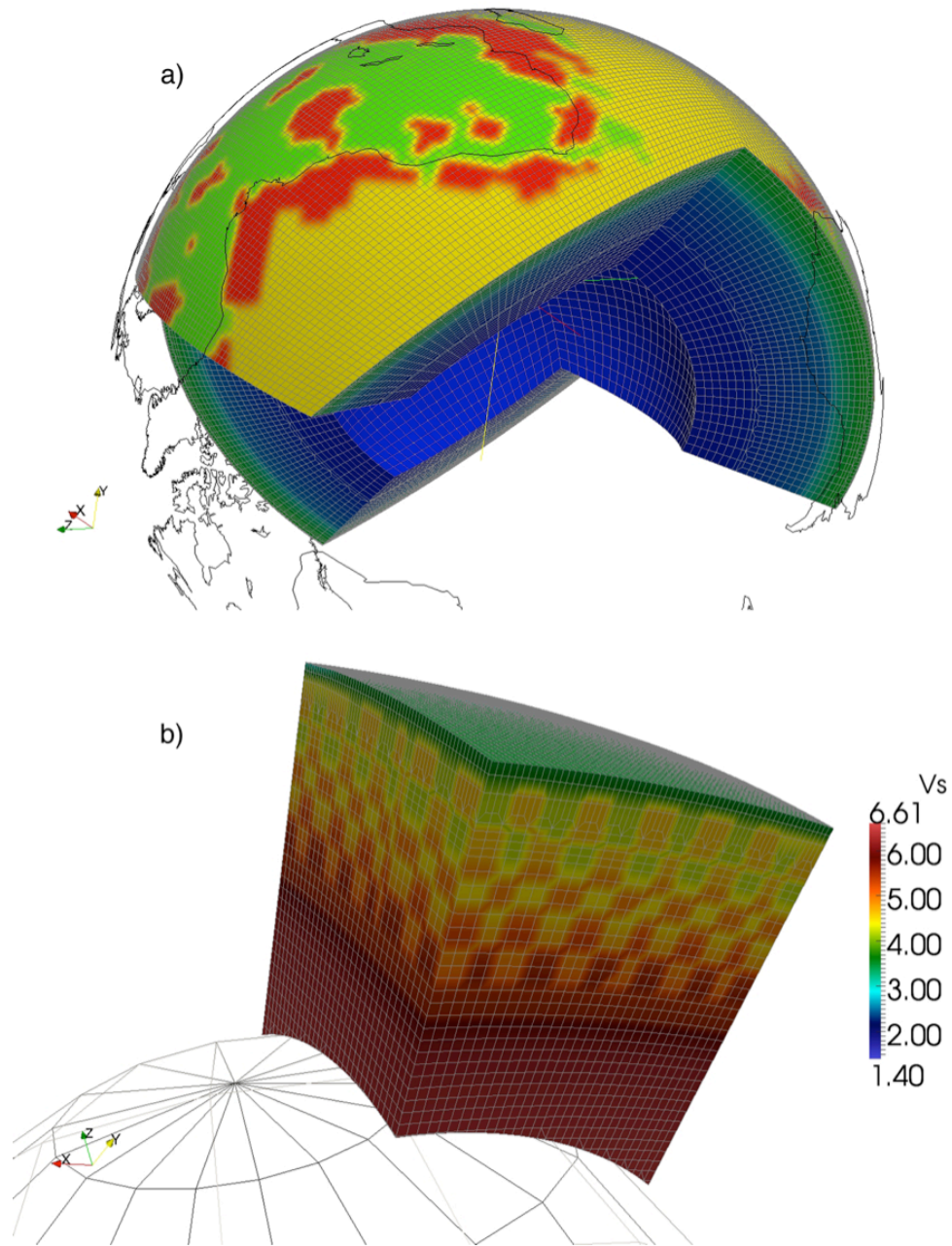
Supp. Figure 3.1. An example of meshes used in synthetic seismogram calculations. a) 3-chunk-earth model, b) The checkerboard earth model implemented in the model in (a). In this case, checkerboards are 2°x2°x100 km, and wave speed variation is ±5% of PREM.

68
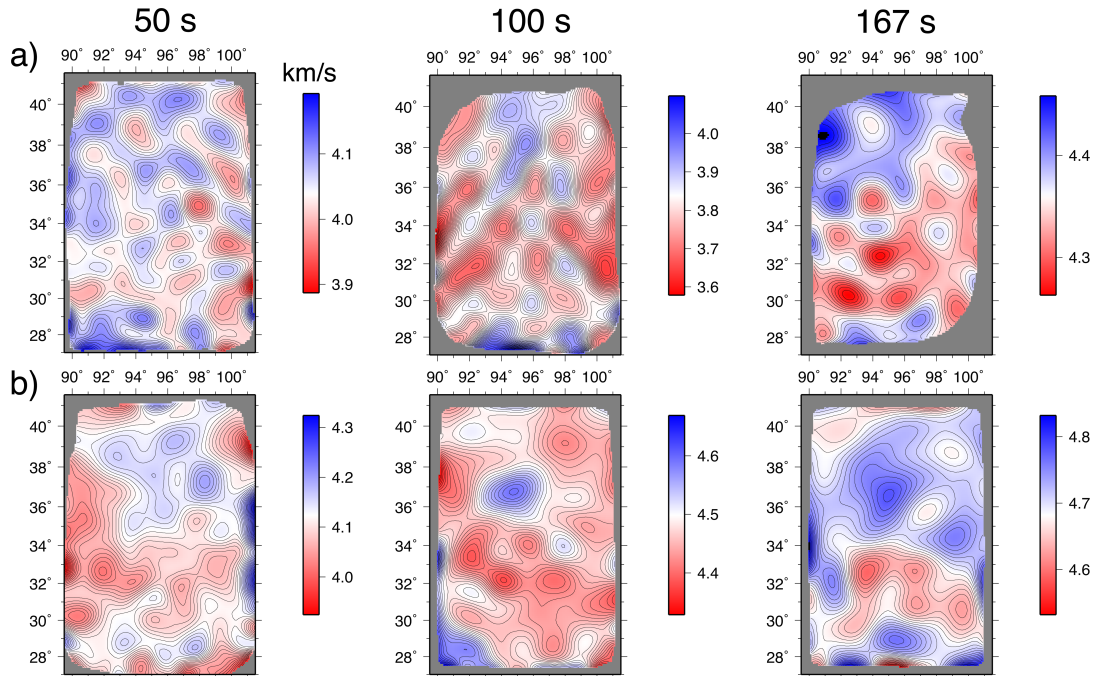
Supp. Figure 3.2. Examples of phase maps for a) Rayleigh, and b) Love waves, for 50, 100, and 167 s periods.
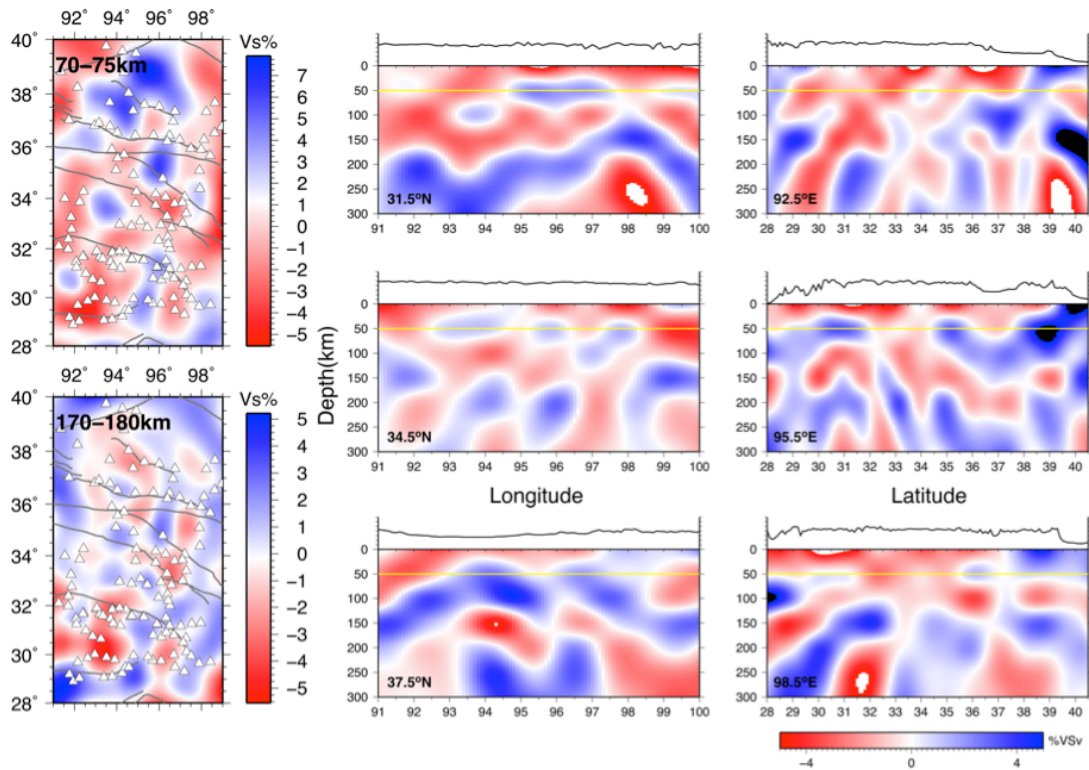
Supp. Figure 3.3. SV resolution results for smaller anomalies (1°x1°x50km).
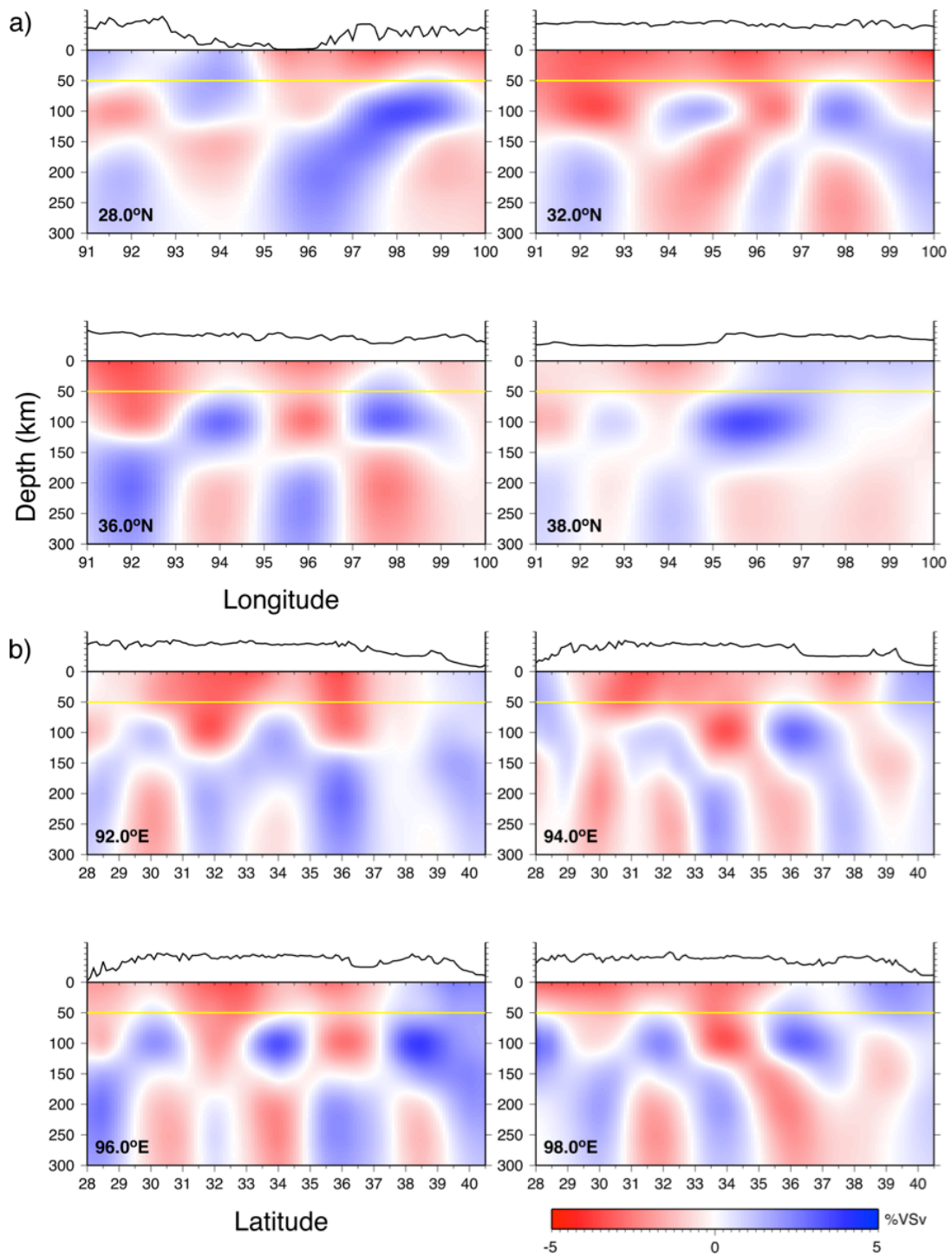
Supp. Figure 3.4. Additional cross-sections for SV wave resolution tests. The coordinates are indicated at the lower left corner of each panel.
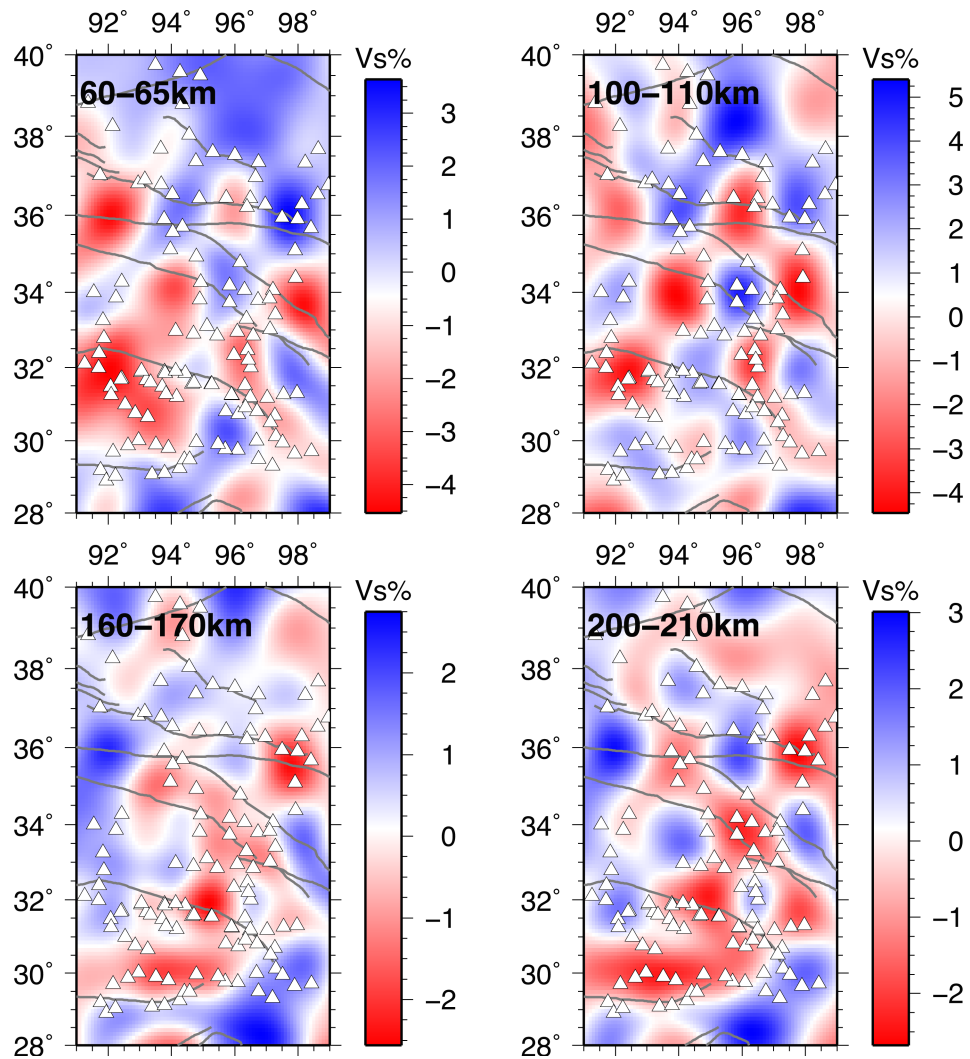
Supp. Figure 3.5. Map views of resolution tests for SV waves for depths 60-210 km. The anomaly sizes are 2°x2°x100 km in the synthetic earth model.
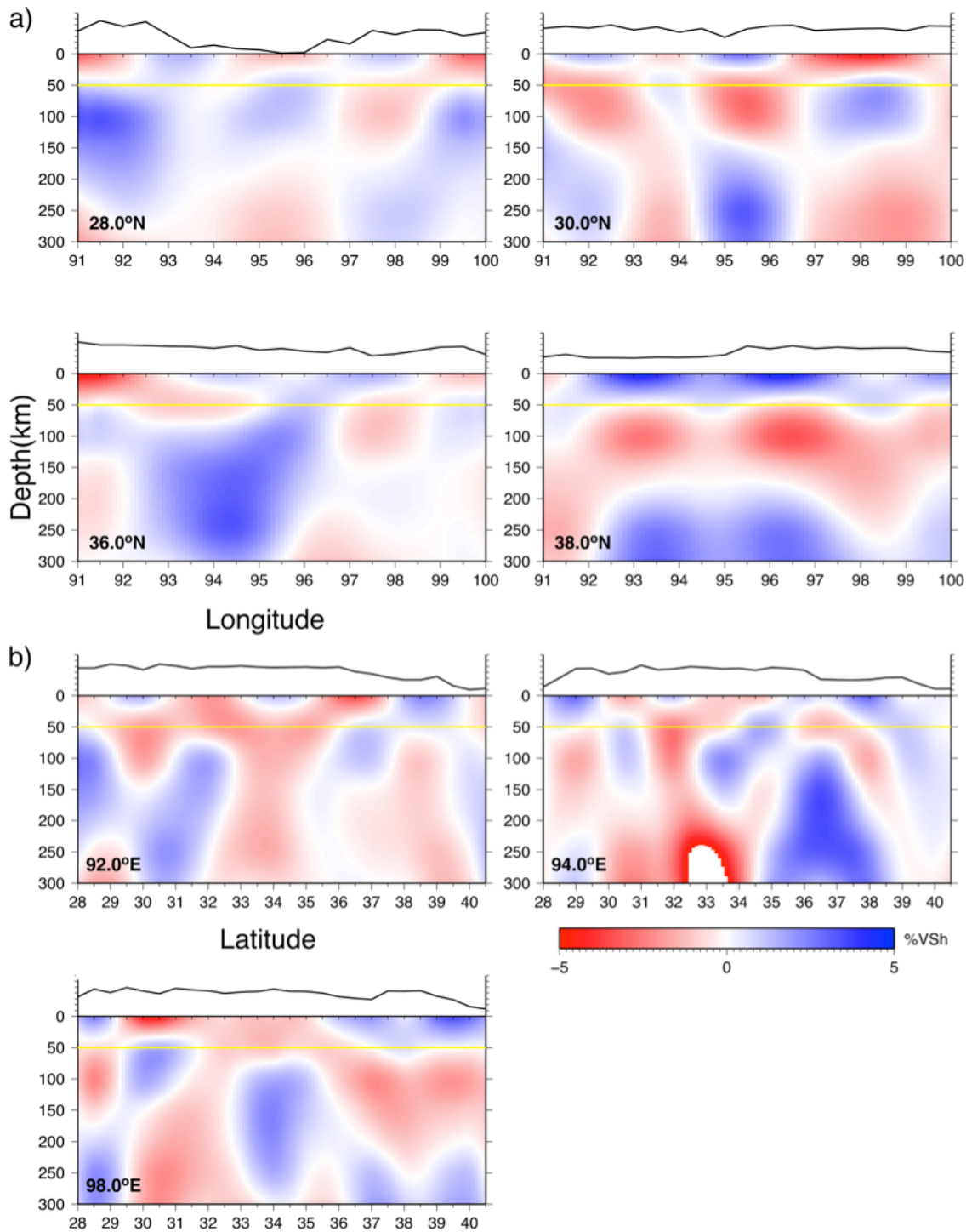
Supp. Figure 3.6. Additional SH wave cross-sections along a) latitudes, and b) longitudes. The coordinates are indicated at the left lower corner of each panel.
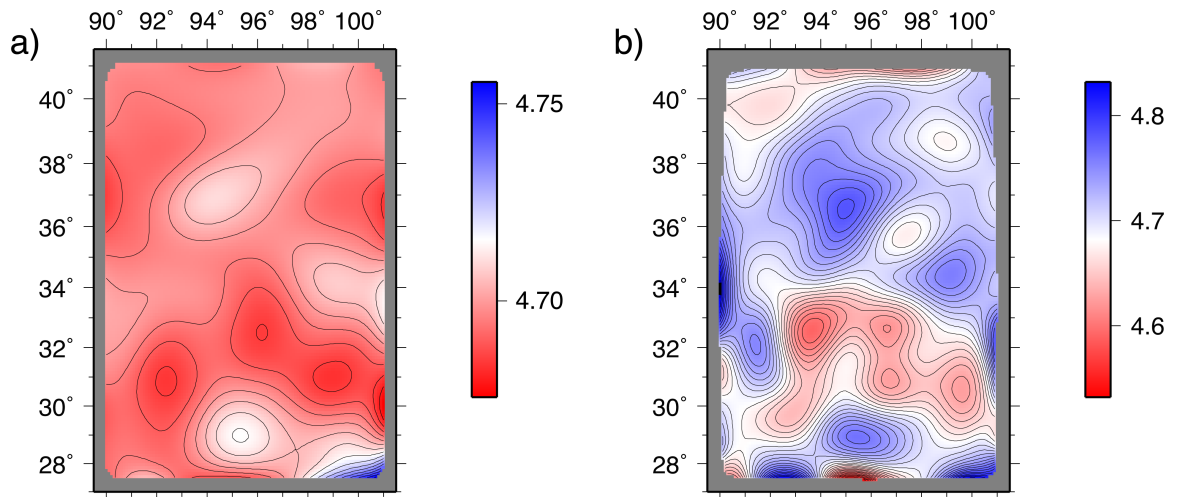
Supp. Figure 3.7. Comparison of phase maps for the period of 167 s using noisy data (S/N=10) and less noisy data (S/N > 15). Note the differences of perturbation range between two phase velocity maps due to seismic noise.

Chapter 4: Conclusions

To better understand the lithospheric structure beneath the E. Tibetan Plateau and constrain the geodynamic models explaining the growth and dynamics of the region, I applied two-plane wave tomography (TPWT), using Rayleigh waves. I calculated anisotropic phase wave speeds and shear wave structure beneath the Plateau (Figure 4.1). My major conclusions are as follows:
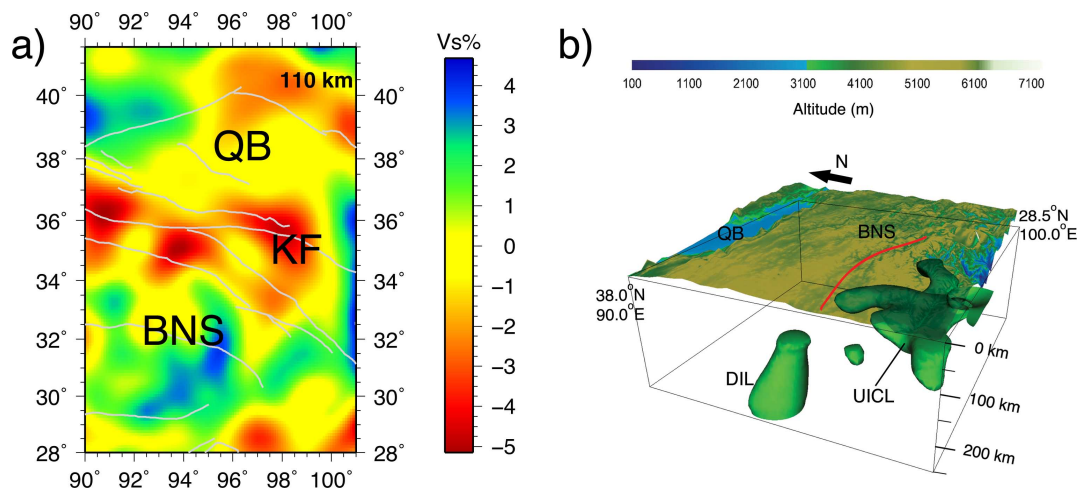
Figure 4.1. a) SV wave anomaly map at 110 km, and b) 3D isosurface of Indian lithosphere. QB: Qaidam Basin, KF: Kunlun Fault, BNS: Bangong-Nijuang Suture, DIL: Detached Indian lithosphere, and UICL: Underthrusting Indian continental lithosphere. The isosurface is created using 2% faster shear wave speeds.

Starting from south of Bangong-Nijuang Suture (BNS), my tomographic models reveal a high velocity body down to ~170 km, beneath the Lhasa and Qiangtang terrains. This feature has a very heterogeneous geometry in east-west direction (Figure 4.1). In my

study, I consider two possibilities for explaining this observation: 1) a possible delamination of Asian lithosphere, and 2) underthrusting of Indian lithosphere.

Considering the compelling evidence from the prior studies (e.g. Tilmann et al. [2003]), I interpret this anomaly as the underthrusting continental Indian lithosphere (UICL). My results indicate that the UICL underthrusts Eurasia sub-horizontally, and contrary to the wholesale underthrusting model [*Barazangi and Ni*, 1982; *Zhou and Murphy*, 2005], does not extend much further north of BNS. Moreover, I suggest that it is laterally torn into at least two wings at ~100 km depth. One plausible mechanism which could explain this fragmentation is increase in extensional stresses due to oroclinal bending along the Eastern Himalayan Syntaxis and oblique collision between India and Eurasia, consequently causing UICL to deform laterally. However, there is no observation of normal faulting east of ~92°E, suggesting either UICL may not be mechanically segmented completely or fragmentation is a recent event. Furthermore, I speculate that flattening of UICL may also have an influence on fragmentation: In reality, UICL is a spherical feature. Due to the decrease in the radius of the earth during underthrusting, flattening of UICL at ~70 km may also induce extensional stresses.

Another high velocity body observed in my models is located ~100 km north of BNS beneath the Qiangtang Terrane, and between ~32°-34°N and 91°-92°E. Initially, I considered delamination as a possible explanation for this anomaly, as this feature appears to be rather isolated then UICL. In my Rayleigh wave tomography study (Chapter 2), I showed that it is possible to observe a delaminated body at ~80 km depth, assuming a high mantle viscosity (10^{21} Pas). On the other hand, thermal modeling results indicated that a possibly delaminated high velocity feature would have higher

temperatures at its center; hence lower seismic wave speeds. Due to the anomaly's

vertical orientation, high seismic velocity similar to UICL and geometry, I conclude that

this anomaly is the westernmost fragment of UICL, which is detached and sinking into

astenosphere.

Further north, beneath Songpan-Ganzi and N. Qiangtang, I observe velocities ~4-

4.2% slower than those beneath Lhasa. The pattern of these low velocity bodies

correlates well with active faults (e.g. northern and southern branches of the Kunlun

Fault). Additionally, this region also has the highest amplitude azimuthal seismic

anisotropy, which is consistent with high strain rates [*Gan et al.*, 2007]. Both viscous

strain heating [*Kincaid and Silver*, 1996] and small-scale convection due to

underthrusting [*Tilmann et al.*, 2003] models fit these observations well. Due to the

indentation of Indian plate and clockwise small-scale mantle flow beneath the plateau

[*Tilmann et al.*, 2003], olivine minerals may align parallel to the direction of elongation,

also indicating the direction of maximum finite strain. According to my seismic

anisotropy results, seismic fast directions are consistent at depth, suggesting vertically

coherent deformation of crust and lithospheric mantle [*Silver*, 1996].

Finally, my shear wave maps reveal a continuous low velocity zone extending to

lithospheric depths beneath the northern branch of the Kunlun Fault. I do not observe any

high velocity bodies that indicate southward continental subduction [*Kind et al.*, 2002] or

underthrusting [*Zhao et al.*, 2011], south of Qaidam Basin.

Second part of my research focuses on more theoretical aspects of TPWT. Here, I

tested the method's resolution and its applicability to Love waves using synthetic

seismograms. My resolution tests are very significant for studies employing TPWT, as

using synthetic seismograms is the most realistic approach for measuring the method's resolution. Additionally, my conclusions in Chapter 3 can be generalized for seismic arrays with similar inter-station spacing.

My studies clearly show that TPWT can resolve SV anomalies at an order of 2°x2°x100 km, down to depths of ~200 km using Rayleigh waves. Below these depths, anomalies are vertically smeared. However, I could not retrieve smaller anomalies successfully. These results prove that anomalies smaller than the dominant wavelength of surface waves can be recovered by TPWT, where traditional approaches break down. Further, I show that a modified version of TPWT can be applied to Love waves, providing sufficient resolution down to ~100 km. However, both vertical and lateral smearing is more evident in SH results, possibly due to shallower depth sensitivity and longer wavelengths of Love waves.

In conclusion, according to my tomographic images, UICL does not extend much further north of BNS. Hence wholesale underthrusting model is not supported by my findings. I see no evidence for southward continental subduction, south of Qaidam Basin. Beneath the central part of study area, my results support the vertically coherent deformation model, as I observe consistent clockwise rotation in seismic fast directions at all frequencies. My studies on lithospheric structure beneath E. Tibet provide further evidence for improving the geodynamic models. Through findings from my resolution tests, we are able to better constrain my measurements to obtain more accurate results. My ongoing research aims to calculate radial anisotropy beneath the region. Combining these results with the azimuthal fast directions from Rayleigh waves (Chapter 2), I will infer 3D anisotropic structure beneath the Plateau.

4.1. References

Barazangi, M., and J. Ni (1982), Veolocities and propagation characteristic of Pn and Sn beneath the Himalayan arc and Tibetan plateau: Possible evidence for underthrusting of Indian continental lithosphere beneath Tibet, *Geology*, *10*, 179-185.

Gan, W., P. Zhang, Z.-K. Shen, Z. Niu, M. Wang, Y. Wan, D. Zhou, and J. Cheng (2007), Present-day crustal motion within the Tibetan Plateau inferred from GPS measurements, *Journal of Geophysical Research*, *112*(B8), doi:10.1029/2005jb004120.

Kincaid, C., and P. Silver (1996), The role of viscous dissipation in the orogenic process, *Earth and Planetary Science Letters*, *142*, 271-288.

Kind, R., et al. (2002), Seismic images of crust and upper mantle beneath Tibet: evidence for Eurasian plate subduction, *Science*, *298*(5596), 1219-1221, doi:10.1126/science.1078115.

Silver, P. G. (1996), Seismic anisotropy beneath the continents: Probing the depths of geology, *Annu. Rev. Earth Planet. Sci.*, *24*, 385-432, doi:10.1146/annurev.earth.24.1.385.

Tilmann, F., et al. (2003), Seismic Imaging of the Downwelling Indian Lithosphere Beneath Central Tibet, *Science*, *300*(5624), 1424-1427.

Zhao, W., et al. (2011), Tibetan plate overriding the Asian plate in central and northern Tibet, *Nature Geosci*, *4*(12), 870-873, doi:10.1038/NGEO1309.

Zhou, H., and M. Murphy (2005), Tomographic evidence for wholesale underthrusting of India beneath the entire Tibetan plateau, *Journal of Asian Earth Sciences*, *25*(3), 445-457, doi:10.1016/j.jseaes.2004.04.007.

VITA

Savas Ceylan was born in Erzincan, Turkey. He received his BS and MS in Geophysics from Istanbul University, Turkey in 2006 and 2008, respectively. His undergraduate and masters research focused on fractal distribution and simulation of microseismic activity for seismic hazard purposes. During his undergraduate and MS studies, he also worked as a software programmer in various projects. He began his doctoral studies at the Geological Sciences Department of University of Missouri in 2008. His research interests are seismic surface waves, surface wave tomography and fractals in geophysics. Starting from February 2014, he will continue his academic career as a Research Fellow at the University of Southampton, UK.